



Catalogue of Strong Nonlinear Surprises in ocean, sea-ice, and atmospheric variables in CMIP6

Joran R. Angevaare¹ and Sybren S. Drijfhout^{1,2,3}

¹Royal Netherlands Meteorological Institute (KNMI), de Bilt, The Netherlands

²Institute for Marine and Atmospheric Research, Utrecht University, Princetonplein 5, 3584 CC Utrecht, The Netherlands

³Ocean and Earth Science, National Oceanography Centre Southampton, University of Southampton, Southampton, SO14 3ZH, UK

Correspondence: Joran R. Angevaare (joran.angevaare@knmi.nl)

Abstract. The Coupled Model Intercomparison Project Phase 6 (CMIP6) archive was analysed for the occurrence of Strong Nonlinear Surprises (SNS) in future climate-change projections. To this end, we built an automated detection algorithm to identify SNS in a reproducible manner. Two different types of SNS were defined: abrupt changes measured over decadal timescales and slower state transitions, too large to be explained by the forcing without invoking strong internal feedbacks in the climate system. Data of 54 models were analysed for five shared socio-economic pathways for ocean, sea ice, and atmospheric variables. The algorithm isolates regions of at least 10^6 km^2 and utilizes stringent criteria to select SNS. In total 73 SNS were found, divided in 11 categories of which 4 apply to abrupt change and 7 to state transitions. Of the identified SNS 45% relate to sea-ice cover, 19% to ocean currents, 29% to mixed layer depth, and 7% to atmospheric systems like the Intertropical Convergence Zone. For each category, probability density functions for time-windows of maximal change indicate SNS occurring earlier and at lower global temperature rise than assessed in previous reviews, in particular the ones associated with winter Arctic Sea ice disappearance, northern North Atlantic winter mixed layer collapse and subsequent transition of the Atlantic Meridional Overturning Circulation (AMOC) to a weak state in which the cell associated with North Atlantic Deep Water involved has vanished. This catalogue emphasizes the possibility of SNS already below 2°C of global warming, even more than the previous assessments based on CMIP5 data.



15 1 Introduction

Based on a literature review and an expert elicitation workshop the concept of Climate Tipping Points was introduced and formalized by Lenton et al. (2008). They recognized that elements of the Earth System can qualitatively change their mode of operation when passing a critical threshold, the latter being popularized as a tipping point. Recent updates of this overview were given in Armstrong McKay et al. (2022), relating the possible tipping to the 1.5 °C global warming threshold, and in
20 Loriani et al. (2023) based on a new assessment by a team of experts. After 2008 a large body of literature appeared discussing specific climate tipping points and subsequent socio-economic tipping points, associating the climate tipping point concept with anthropogenic climate change, its impacts and risks, and policy (Kopp et al., 2025). Ref (Kopp et al., 2025) strongly criticized the tipping point concept, arguing it oversimplified the complex dynamics of the Earth Systems (tipping elements) involved, and would be counterproductive in terms of adequate policy reactions to global warming, because in their words
25 “Climate change is already causing demonstrable and obvious harm around the world. Tipping point discourse to the contrary, there is no specific increment of temperature increase that science can identify as the boundary between our current, already-dangerous climate and a future catastrophic climate, and no justification for doomism and paralysis while the world continues to warm.”

In the latest Report (AR6) of the Intergovernmental Panel for Climate Change (IPCC), the focus was slightly altered from
30 tipping points to potential abrupt and irreversible change of Earth System elements (Lee et al., 2021), although the related definition of a tipping point was also used, recognizing the difficulty in proving the existence of a tipping point other than in often simplified climate or Earth System element models. One step earlier than what now can be seen as the “tipping point controversy” was taken in Drijfhout et al. (2015), where a catalogue of abrupt changes occurring in simulations of the Climate Model Intercomparison Project Phase 5 (CMIP5) (Taylor et al., 2012) was presented. The naming “abrupt shifts” was chosen
35 deliberately, to avoid discussion whether a tipping point was involved, and if so, where the tipping point exactly was located.

Since Drijfhout et al. (2015) a new CMIP6 has been carried out and a new IPCC AR6 Report has been written, and it seems pertinent to also develop a new catalogue based on CMIP6 simulations. These simulations are driven by new emissions and land use scenarios based on new pathways of societal development (shared socio-economic pathways or SSPs) (O’Neill et al., 2016). CMIP6 simulations thus differ from previous CMIP projections, being produced with updated climate models as well as
40 being driven with updated emissions and land-use scenarios. In addition, because new updates and overviews of tipping points have been published since CMIP5 (Armstrong McKay et al., 2022; Loriani et al., 2023) it seems pertinent to benchmark these overviews with how CMIP6 models simulate the associated events. Also, a recent paper by Terpstra et al. (2024) followed a slightly different approach and applied Canny edge detection (Canny, 1986) to CMIP6 data from model simulations forced with the rapid 1ptCO₂ (1 % annual CO₂ increase) scenario, similar to the work of Bathiany et al. (2020) who applied similar
45 methods to CMIP5 data. Apart from comparing our results with those of Terpstra et al. (2024), it is of interest to investigate whether CMIP6 models support recent publications on approaching tipping points for e.g. the Atlantic Meridional Overturning Circulation (AMOC) (Boers, 2021; Ditlevsen and Ditlevsen, 2023).



Here, we follow the same philosophy as in Drijfhout et al. (2015) and to avoid confusion about applying the term “abrupt change” to changes that involve a qualitative change in mode of operation but evolve over many decades, we will coin here the name Strong Nonlinear Surprises (SNS), as from CMIP runs we cannot deduce whether these SNS involve the passing of a critical threshold, or tipping point, or whether the SNS is reversible and if so, on which timescale. New with respect to Drijfhout et al. (2015) is that, with improved computer power and developments in the realm of Machine Learning, we have been able to adjust the method of finding and classifying SNS used in Drijfhout et al. (2015), to become fully automatic and reproducible. It should be noted that the classification criteria themselves always will contain an element of subjectivity that is open for discussion or adjustment, as there exists no fundamental theory or set of equations that uniquely defines those criteria. Instead, they are motivated to capture well-known tipping points as defined in the literature (e.g., (Armstrong McKay et al., 2022; Loriani et al., 2023)), to detect model behaviour that is truly surprising and features large changes in climate variables and climate elements that are truly outstanding, but at the same time limits the total amount of such events to a manageable number. In addition, using our automated and reproducible method other users can simply adjust these criteria to their own preference.

Also new is that for each SNS we indicate the moment (time window) of maximum change, depending on the timescale of smoothing applied to the relevant time series and timescale over which the change is calculated. Using this method, we are able to give a probability density function (PDF) for each SNS for each model describing the likelihood of maximum change, which we average over all models in each category to obtain the full PDF of that category. With this approach we aim to prevent our results becoming subject to a politicized scientific debate and to avoid pitfalls of oversimplifying the concept of thresholds which, after being exceeded, would turn climate change into a new category of harmfulness. However, we do believe that SNS imply elements of climate change that generally contain larger, potentially more harmful changes than anticipated from current ongoing changes in climate. cataloguing these changes as they occur in climate simulations, together with their projected timing of maximum change, should be of interest to the climate science community, as well as for a wider audience including policymakers. However, we emphasize, and discuss per case when relevant, that climate models contain severe biases and errors, and that both the type of SNS as well as its timing is subject to large uncertainties and often model-dependent. But if they do occur in model simulations, the implication often is that they might occur in nature as well and should be reckoned with.

This paper is organized as follows: In section 2 (methods) we define the categories of SNS and how they are found. Details of the classification criteria have been moved to the Appendix, also containing tables and supporting figures. In section 3 the SNS are discussed and illustrated per category and model simulation in which they appear. Section 4 contains a discussion focusing on robustness of our results, followed by conclusions (section 5).

2 Methods

In our method we focus on decadal-timescale changes of yearly mean values and discern two types of SNS: abrupt changes and transitions to a new equilibrium. The precise criteria may depend on the variable involved and the length of the time series



investigated. Additionally, we have chosen to do this in an automated and reproducible manner to improve replicability. To achieve this, we follow a phased approach as in Drijfhout et al. (2015), but the three phases identified in that paper are now combined in one workflow without relying on visual inspections as in Drijfhout et al. (2015). The phases are schematically depicted in Figure 1.

85 We applied this method to data of 54 models using the SSP119, SSP126, SSP245, SSP370, and SSP585 scenarios and all available ensemble-members. We investigated 12 CMIP6 variables in this study (see Table A1): hfds (Downward Heat Flux at the Sea Water Surface), mlotst (Ocean Mixed Layer Thickness Defined by Sigma-T), msftbarot (Ocean Barotropic Mass Streamfunction), msftyz (Ocean Meridional Overturning Mass Streamfunction), msftmz (Ocean Meridional Overturning Mass Streamfunction), siconc (Sea-Ice Area Percentage on ocean grid), siconca (only if siconc is not available, Sea-Ice Area Per-
90 centage on atmospheric grid), sos (Sea Surface Salinity), tas (Near-Surface Air Temperature), tos (Sea Surface Temperature), wfo (Water Flux into Sea Water) and zos (Sea Surface Height Above Geoid). We focused on these ocean, sea-ice, and atmospheric variables as they were the largest contributor to the SNS in Drijfhout et al. (2015), catalogues for SNS in other variables will follow in a separate paper. The variables msftyz, msftmz are used to identify SNS in the AMOC. These variables have a different format from other (surface) variables and are therefore handled differently (as discussed in (Drijfhout et al., 2024a)).

95 As shown in Figure 1, we take the following steps to identify SNS. First, monthly CMIP6 data are averaged to obtain yearly data¹. Thereafter, the data are re-gridded to a Gaussian N90 grid using cdo (Schulzweida, 2023). We also combine the historical run with the scenario runs to obtain a dataset that spans the years 1850 to 2100 or later. We split the ocean and land fractions of the data and evaluate both separately as several features used below or in subsection A1 may greatly differ above ocean and land. In this catalogue, this is only relevant for TAS as all other variables are only ocean variables.

100 In the second step, we isolate regions using four different approaches. The aim of each approach is to isolate regions that have a higher likelihood of showing an SNS, which will be evaluated in the next phase. The region-isolation only serves to reduce the computational complexity and is therefore designed to rather select too many than too few regions. For this step, we use the scenario run only (years 2015 to 2100 or later) and select regions that are at least 10^6 km^2 . The first region-finding approach selects regions that have a large difference between their start and end values. In this approach we select regions that surpass
105 a percentile threshold T . To avoid selecting too large regions, we first try a very high threshold of $T \geq 99.99\%$. We select all resulting regions that surpass this threshold and span at least 10^6 km^2 . We then select regions (that were not selected in the previous iteration) that surpass $T \geq 99.74\%$ (and are $\geq 10^6 \text{ km}^2$). We keep repeating this process for successively lower values of T until (after a total of 61 iterations) we select regions with the lowest threshold $T \geq 85\%$. Regions ($\geq 10^6 \text{ km}^2$) where
110 $T < 85\%$ are not selected. In other words, we repeat the process for a total of 61 values of T , which are linearly spaced between 99.99 % and 85 %. The second approach computes the percentiles of the standard-deviation of the (linearly) detrended time series of 10-year running mean (σ_{det}) and the 10-year maximum jump of the 10-year running mean (MJ_{10}). Both percentiles must lie above the percentile threshold T , which is linearly spaced between 99.99 % and 85 % in 61 steps. The third approach is very similar to the second, and multiplies the percentile scores of σ_{det} and MJ_{10} and then selects regions where this product is

¹Except for mlotst, where we took the maximal value from monthly data as the yearly maximum is more relevant for deep convection than the yearly average.

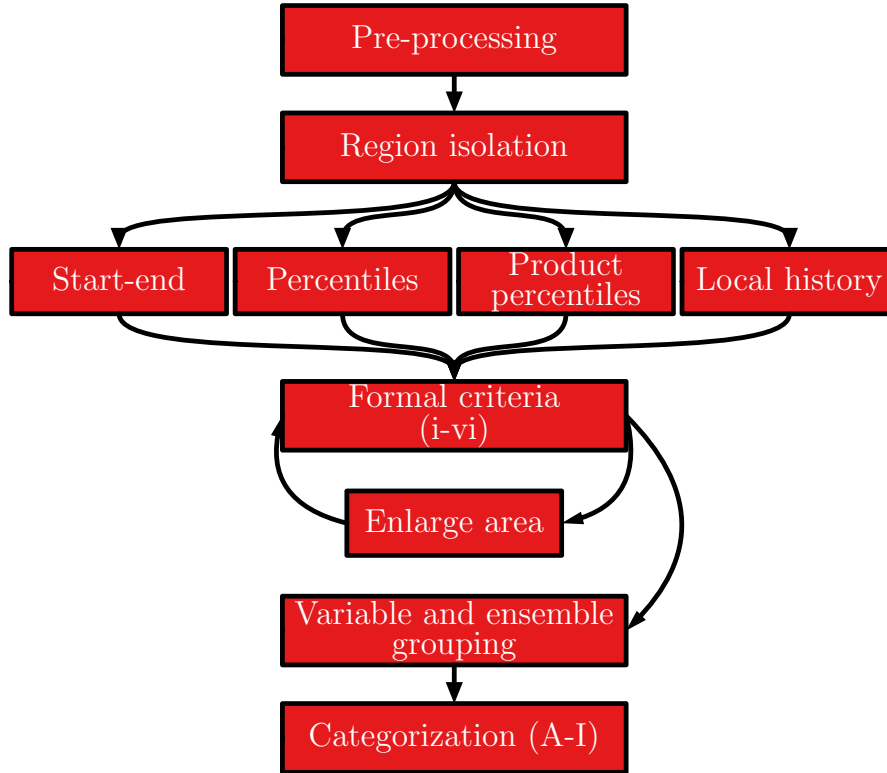


Figure 1. The workflow that leads to SNS identification. At the first phase, monthly CMIP6 data is pre-processed by calculating annual means and regridding any of the original coordinate systems to a gaussian N90 grid. At the next step, promising regions are isolated based on four algorithms (see text), which are subsequently evaluated using formal criteria to identify the regions with an SNS. Regions where an SNS occurs are enlarged by merging with adjacent or overlapping regions or groups of $5^\circ \times 5^\circ$ square regions. Finally, we first group the SNS by combining ensemble-members and variables of one model that occur in overlapping regions and then manually categorize these SNS into 11 categories.

above threshold T_p , which is linearly spaced between 99.9 % and 85 %. Finally, the last approach compares the values of σ_{det} and MJ_{10} with the values in the preindustrial-control, henceforth pi-control dataset. The ratio of the scenario values divided by the respective pi-control values has to surpass a threshold of T_{PiC} , linearly spaced between $8\times$ and $2.5\times$ in 61 steps. The region isolation phase isolates $\mathcal{O}(10 - 100)$ regions of at least 10^6 km^2 are often adjacent and may overlap when found by different methods.

In the third phase, we evaluate if a region from the previous phase fulfils formal criteria. If this is the case for a given region, any adjacent or overlapping regions are merged with it, as long as the combined region also fulfils the formal criteria. Additionally, to flexibly increase the size of an identified region, we also attempt merging adjacent $5^\circ \times 5^\circ$ regions (again, as long as the combined region also fulfils the formal criteria).

These strict requirements formalize the role of expert judgment of earlier work (Drijfhout et al., 2015). The formal criteria are designed to select the following types of events:

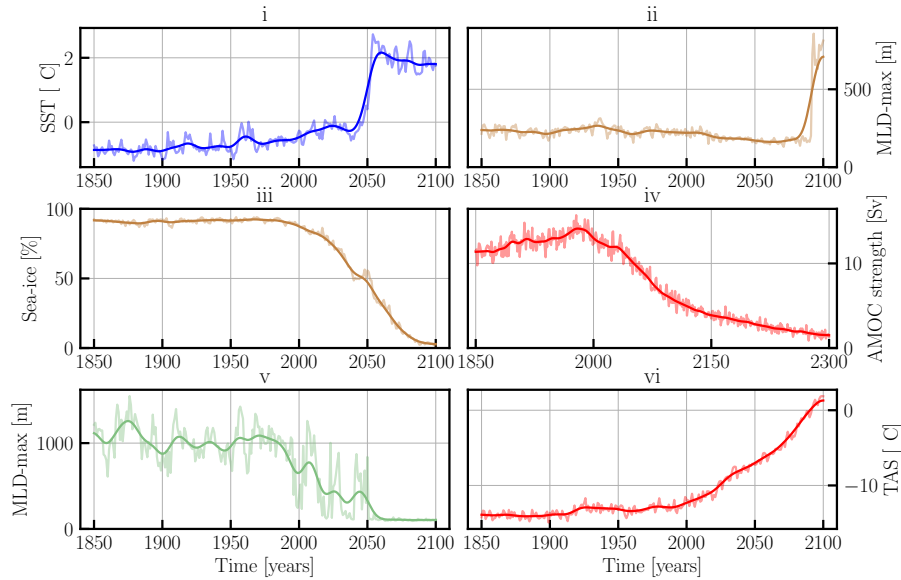


Figure 2. Examples of the six formal classification criteria (i-vi), see text for further details. Panels i, ii, iii, iv, v, and vi refer to SNS 61, 60, 6, 50, 66, and 18 respectively in Table A3. The solid lines indicate the smoothed yearly time series (which are illustrated as shaded lines). The data is smoothed using a Lowess filter with a window of 40 years.

- 125 (i) Abrupt change.
- (ii) Abrupt change (at the end of a dataset).
- (iii) Almost complete disappearance of sea-ice in an area of at least $5 \times 10^6 \text{ km}^2$.
- (iv) Transition to an extremely weak state in the Atlantic meridional overturning circulation (AMOC)².
- (v) Transition from a deep to an extremely shallow ocean mixed layer, or vice versa.
- 130 (vi) Transition to a completely new state in other ocean/atmosphere variables.

An example of a time series associated with each criterion is shown in Figure 2. Generally, i and vi are generic criteria for abrupt changes and state transitions respectively. Criterion ii selects abrupt SNS that are otherwise missed by criterion i if the occurs and at the end of the dataset. Criteria iii specifically addresses the state transition of large-scale, almost Arctic-wide sea-ice loss, as almost all models will feature at least a peripheral region of sea-ice loss under climate change when naively
 135 applying criterion iv. Criterion iv aims to detect state transitions in msftyz, msftmz which cannot be selected by criterion vi because of their different data structure. Criterion v selects state transitions in the yearly maximum of the mixed layer depth. Because mixed layer depth is an ocean variable largely driven by fast atmospheric changes, it often features large variability on decadal timescales, much larger than other ocean variables, which makes criterion vi less applicable. Criterion vi selects

²As discussed above, this criterion follows the methodology described in Drijfhout et al. (2024a) to isolate SNS rather than the workflow as in Figure 1.

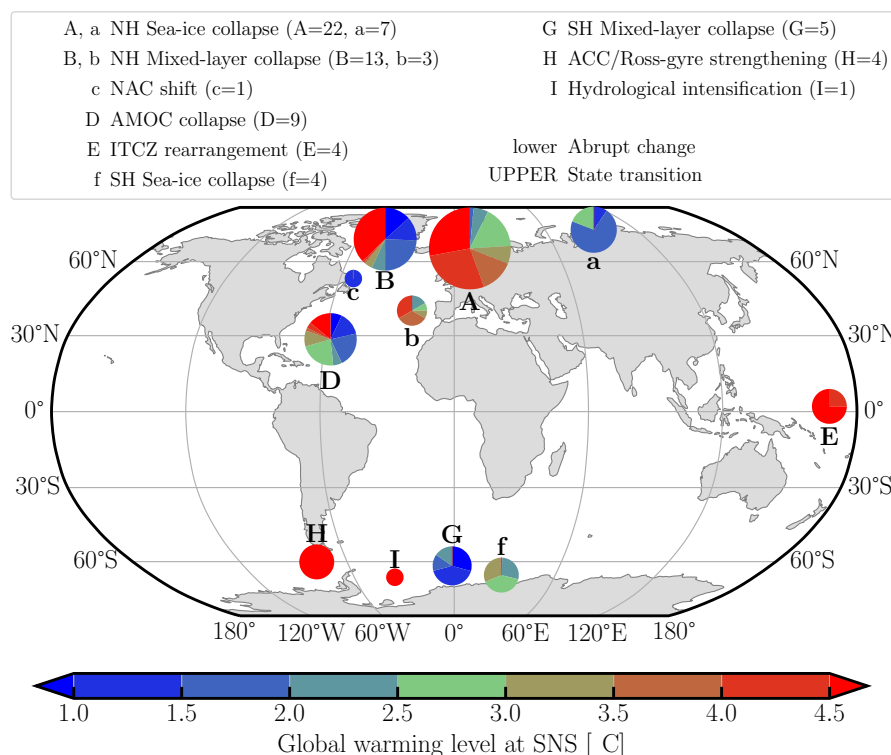


Figure 3. Overview of strong nonlinear surprise categories. Capital letters denote large state transitions, while lowercase letters indicate abrupt changes. If a physical process causes both state transitions and abrupt changes in the same region, the same letter is used (e.g. A and a). The pie-charts are scaled in size to the number of models in which the pertinent SNS are found (corresponding to Table A3). The associated colours show the average global warming level with respect to 1850-1880 during the 30 years period where the change is greatest, see text for more details.

state transitions in all other variables than criteria iv and v. The equations related to each of the six criteria are available in the appendix (subsection A1). We evaluate the formal criteria for each variable and each ensemble-member available in our dataset. In Table A2 we list all the investigated datasets. After combining ensemble-members, variables, and scenarios that overlap, we end up with 73 SNS, as will be discussed in section 3. We group the 73 SNS into 11 categories (as in Figure 3) by combining cases of different models that are in the same region and occur because of the same underlying physical processes.

3 Results

Figure 3 illustrates the locations of the 11 categories (A-I). Some categories have related abrupt change and state transition SNS, for which we use the same uppercase letter for their state transitions and lowercase letters for abrupt changes to highlight their relation. The position of each of the pie-charts in Figure 3 is indicative of the mean global position of the SNS in that category. Each pie-chart roughly indicates the global warming level at the time of the maximum change. For simplicity, we take the time where the 30-year change in the 10-year running mean of the time series of each SNS is largest. We relate this



150 time to a global warming level relative to the reference period of 1850-1880. We then calculate the average temperature for each case belonging to the respective category. Some SNS (e.g. #36 in Table A3) may be manifested in multiple variables, ensemble-members and SSPs and therefore have to be normalized. This way, we equally weight each individual case within each category.

Figure 3 emphasizes the relative number of models that features a certain category of SNS, as the size of each pie-chart is scaled to the number of SNS. Below, we discuss each of the physical processes associated with these SNS one by one. We follow an order that groups physical processes, rather than the alphabetical order of Figure 3.

3.1 Abrupt year-round sea-ice loss in the Arctic, associated with abrupt change in ocean and atmospheric variables (a)

As in Drijfhout et al. (2015), we find a few cases of abrupt sea-ice decrease in the Arctic. These cases are no longer restricted to the SSP585 scenario, as in CMIP5 for the RCP8.5 scenario, but also occur for weaker forced scenarios. Still, the forcing mechanism is in each case the global warming and polar amplification of this signal, mainly caused by the sea-ice albedo feedback. In these cases, (e.g. CanESM5) the trajectory in the SSP126 scenario is qualitatively similar to the transition to a large, year-round ice-free area in the Arctic in the more strongly forced SSP370 and SSP585 scenarios. Before 2050 the change proceeds abruptly but after 2050 it stabilizes unlike the evolution in the more strongly forced scenarios, which become part of Category A transitions (Compare Figure 4 and Figure 5). In this model the time evolution in the SSP245 scenario is somewhere in between the evolution in SSP126 and SSP370, and it also classifies as an abrupt case “a”. A qualitatively similar story holds for other models but depending on the model’s sea-ice sensitivity to global warming, it may occur for stronger-forced scenarios up to the SSP370 scenario when the decrease in sea-ice in those scenarios is too weak to classify as Category A transition. These cases are: CanESM5-1 (SSP119 and SSP245); EC_EARTH3-Veg-LR (SSP126); MIROC6 (SSP126, SSP245 and SSP370); and GISS-E2-1-H (SSP370). In one scenario the abrupt sea-ice loss induces equally abrupt changes in ocean and atmospheric variables, namely TAS (near-surface air temperature) in CanESM5-1 (SSP119).

In Drijfhout et al. (2015) this type of abrupt change was compared to the feedback-driven abrupt shifts in sea-ice edge found in an energy balance model (Rose and Marshall, 2009). Its similarity to the more complete transition to ice-free conditions in more strongly forced scenarios points to anthropogenic warming as the driver, but internal variability may affect the timing of the abrupt event. Hankel and Tziperman (2023) demonstrated the existence of winter (and thus year-round) sea-ice tipping points in a state-of-the-art climate model. In a previous study (Hankel and Tziperman, 2021) they identified a positive feedback cycle in which, at the start of winter, more open ocean water allows for moistening and warming of the lower atmosphere, which in turn increases downward longwave radiation, which reduces ocean freezing. The diminished winter sea-ice growth results in lower surface albedo, leading to increased shortwave absorption during springtime. In addition, increased ocean heat uptake causes even warmer ocean conditions that lead to further sea-ice reduction. Abrupt loss of Arctic sea-ice could also be driven by other positive feedback mechanisms (Abbot et al., 2009; Kay et al., 2012; Feldl et al., 2020)). A curious outlier is the very large surface air temperature increase over the Pacific sector of the Arctic in UKESM-0-LL in its SSP126 scenario, which

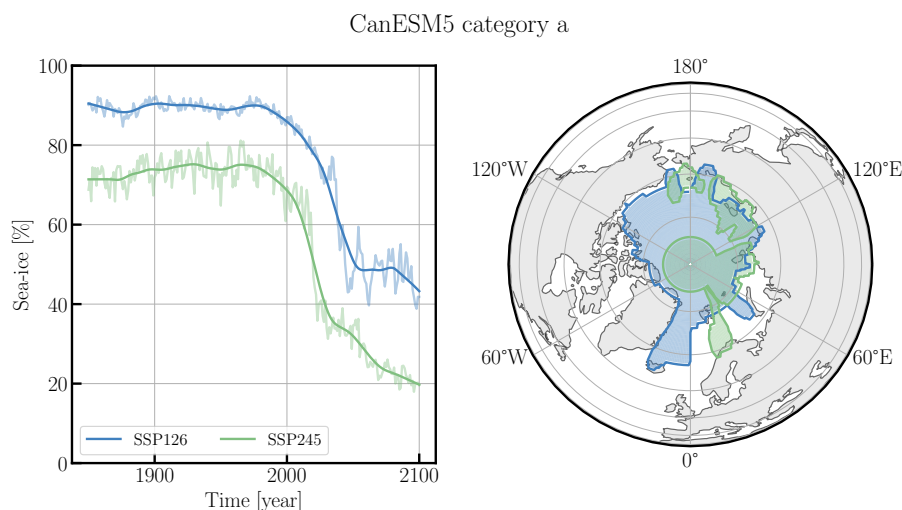


Figure 4. Category “a” for the CanESM5 model (SSP126: r25i1p2f1, SSP245: r1i1p1f1). The left panel shows the yearly averaged time series (shaded) and the smoothed time series (solid), where we use the same smoothing as in Figure 2. The right panel shows the corresponding region.

is clearly driven by sea-ice loss over that area, but the area being too small to classify as a category A transition and not abrupt enough in sea-ice cover either, yet still causes an abrupt change in air temperature.

185 Similarly, there is another case where the mixed layer abruptly increases in the Northern Hemisphere. This occurs in the Arctic where the disappearance of sea-ice allows increases in heat loss to the atmosphere that deepen the yearly averaged mixed layer depth from 50 to 350 m. This abrupt increase in mixed layer depth occurs in CNRM-ESM2-1 in the SSP245 scenario, north of 80° N and ranging from 10-120° E, roughly north of the Barents and Laptev Seas. This typically occurs in an intermediate forcing scenario, strong enough to let sea-ice disappear, but also moderate enough in atmospheric temperature
190 increase, still allowing for substantial heat loss from the ocean to the atmosphere.

3.2 Transition to large, year-round ice-free areas in the Arctic and induced ocean and atmospheric state changes (A)

In Drijfhout et al. (2015) five models were found in which the winter sea-ice cover (siconc) largely collapsed. In CMIP6 many more of such cases appear, namely 21 models and 29 model runs (ACCESS-CM2, ACCESS-ESM1, CanESM5, CanESM5-1, CanESM5-CanOE, CESM2-WACCM, CMCC-CM2, CMCC-ESM2, E3SM-1-0, E3SM-1-1, E3SM-1-1-ECA, EC-Earth3-Veg,
195 FIO-ESM-2-0, GISS-E2-1-H, HadGem3-GC31-LL, HadGem3-GC31-MM, IPSL-CM6A-LR, MRI-ESM2-0, NorESM2-MM, UKESM1-0-LL, UKESM1-1-LL), although it should be noted that we focus on annual mean siconc and allow for arbitrary areas of more than 5 million square kilometres, rather than restricting the analysis to the entire Arctic north of 75° N. In Drijfhout et al. (2015) the Arctic winter siconc collapse only occurred in RCP8.5 extended runs. A model-dependent temperature threshold varying between 4.5 °C and 8.2 °C was needed for the onset of the winter siconc collapse. Such thresholds are much
200 earlier reached in CMIP6 models (Figure 5), see also Angevaere et al. (2025) for further discussion.

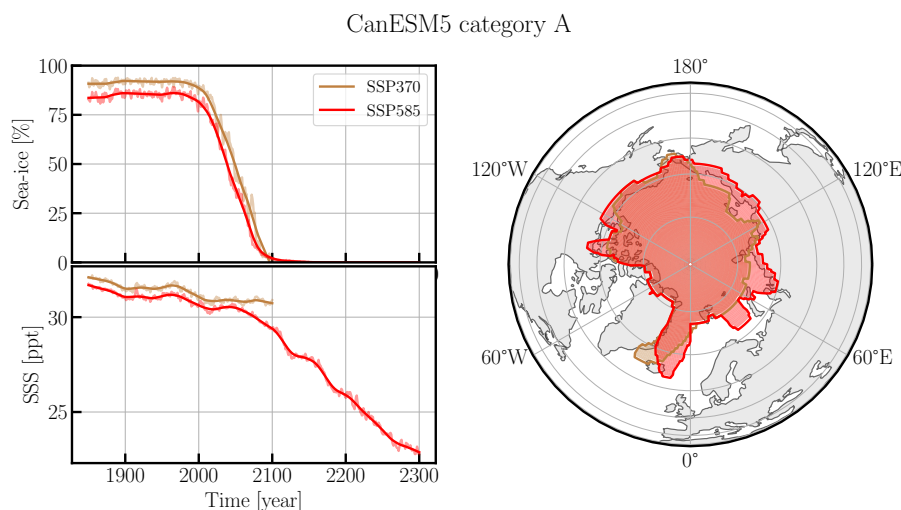


Figure 5. Category “A” for the CanESM5 model (r1i1p1f1), where the SSP370 model run was evaluated until the year 2100 and SSP585 was extended to 2300. The sea surface salinity (SSS) is expressed in parts per thousand (ppt). The region (right) corresponds to the region wherein the sea-ice SNS is found, and, for consistency, the left panels correspond to these regions. For SSP585, an SNS was also found in a (smaller) sub-region for SSS. See caption of Figure 4 for details.

New cases have emerged where one or more ocean variables reach a new state that appears not only driven by global warming but is caused by additional feedbacks (ice-albedo) and dynamical changes. Most of these are state transitions in the Arctic over regions where sea-ice disappears. They appear in ACCESS-CM2 (sea surface salinity; SSS), ACCESS-ESM1-5 (near surface air temperature; TAS), CanESM5 (SSS) see also Figure 5, CESM2-WACCM (SSS and Sea Surface Height; SSH), FIO-ESM-2-0 (TAS), GISS-E2-1-H (SSS), MRI-ESM2-0 (SSS), UKESM1-0-LL (TAS), and UKESM1-1-LL (TAS). In Figure 5 and throughout the remainder of this work, the unit of SSS, parts per thousand, is abbreviated as ppt. In these cases, the disappearance of sea-ice allows for a much stronger ocean-atmosphere coupling with enhanced heat and freshwater exchange that ultimately leads to a completely new ocean and/or atmospheric climate in the Arctic. A similar case is the large transition in TAS that occurs over the Arctic in MIROC6 in its SSP585 simulation, but in this model, the decline in sea-ice cover is too weak to fulfil criterion iii.

3.3 Abrupt year-round sea-ice loss in the Southern Ocean, associated with abrupt change in ocean and atmospheric variables (f)

We find 4 cases of abrupt sea-ice loss in the Southern Ocean. These cases are, like in the Arctic, also forced by global warming, although the polar amplification / warming signal is weaker here. Abrupt sea-ice loss in the eastern Ross Sea and Amundsen Sea occurs in the SSP585 scenario in HadGem3-GC31-MM. Similar abrupt sea-ice loss, but more in the central Ross Sea, is seen in GISS-E2-1-H, accompanied with abrupt increases in upward heat flux and sea surface temperature for both the SSP245 and SSP370 scenarios, likely driven by the onset of deep convection. In the same model also an abrupt sea-ice loss occurs east of the

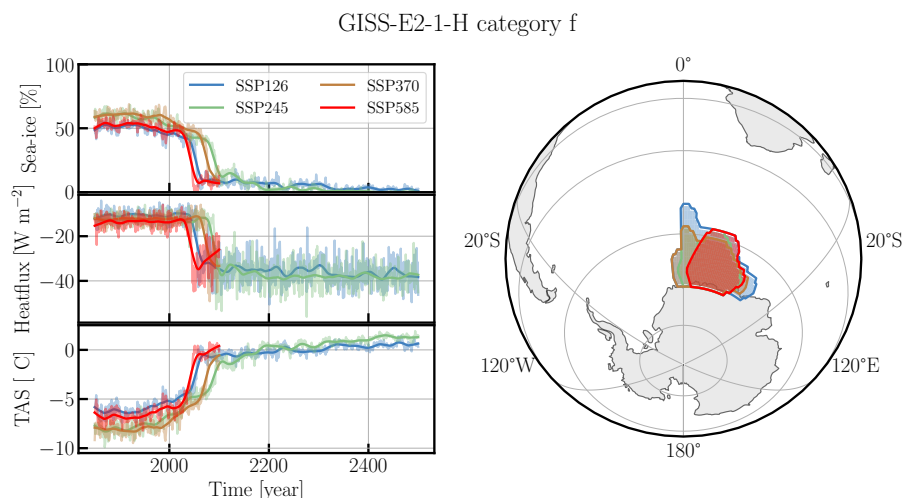


Figure 6. Category “f” for the GISS-E2-1-H model (SSP126: r4i1p3f1, SSP245: r2i1p1f2, SSP370: r3i1p1f2, SSP585: r4i1p3f1). For consistency, the averages (left panels) are calculated over the region (right panel) wherein the sea-ice SNS are detected. See caption of Figure 4 for details.

Weddell Sea (Lazarev Sea) in most scenarios (SSP126, SSP245, SSP370, SSP585) which shows an almost complete collapse of perennial sea-ice there. Subsequent abrupt changes in the Lazarev Sea also occur for ocean and atmospheric temperature and surface heat flux (Figure 6). All these changes seem driven by an onset of deep convection in the Lazarev Sea with abrupt increases in sea surface temperature (SST) and TAS, and an abrupt increase in outgoing heat flux. Depending on the variable, the abrupt change is seen in different scenarios; always in SSP126 but the change in SST is also abrupt in SSP245 and SSP370, and even in SSP119 where sea-ice itself disappears less abruptly. These changes all occur in the second half of the 21st century. A similar scenario for the Lazarev Sea occurs in CESM-WACCM, but the change in that model is only abrupt in sea-ice there in the SSP585 scenario. In Drijfhout et al. (2015) we found one case of an abrupt sea-ice *increase* in the Southern Ocean associated with a halt of deep convection there. Such an abrupt transition is not found in CMIP6.

An abrupt change in mixed layer depth without accompanying abrupt changes in other variables is simulated in the BCC-CSM2 model. Here the yearly averaged mixed layer depth in the Ross Sea, in the middle of the Ross Gyre, suddenly increases from less than 100 to 1000 m between 2090 and 2095 in the SSP370 scenario. This abrupt change is driven by the disappearance of sea-ice, which itself does not occur abruptly. In these cases, an additional feedback occurs between sea-ice disappearance and the onset of deep convection. Such feedback associated with global warming has been demonstrated to occur for the Arctic (Våge et al., 2018), but not (yet) for the Southern Ocean. It should be noted, however, that Morioka et al. (2024) demonstrated this feedback for multi-decadal variability in Southern Ocean sea-ice cover, driven (or triggered) by changes in the Southern Annular Mode, which by changing upwelling of subsurface saline modulates the ocean stratification and can abruptly enhance or onset deep convection there.



3.4 Abrupt Northern Hemisphere winter mixed layer weakening in ice-free areas, associated with abrupt changes in ocean temperature and salinity (b)

In Drijfhout et al. (2015) several cases of abrupt change in Northern Hemisphere deep convection were identified. These were all cases where deep convection and mixed layer depths collapsed. In CMIP6 we do not find any such case. This is in apparent
240 contradiction with Swingedouw et al. (2021) who identified three CMIP6 models in which abrupt cooling events and abrupt transitions to very low mixed layer depths in the North Atlantic subpolar gyre (SPG) occurred. Here, we do not classify those events as abrupt changes, as such changes are ubiquitous in the time series, also occurring in the historical and pi-control runs preceding the abrupt events that in Swingedouw et al. (2021) are identified (see their Figures 1 and 6). This is partly due to the more stringent classification criteria we apply, and due to the very large internal variability in mixed layer depth,
245 making it difficult for mixed layer changes to classify as abrupt without relaxing the criteria for mixed layer depth relative to other variables. Also note that Swingedouw et al. (2021) classify their abrupt events by demanding the associated temperature change to exceed a certain threshold. We, however, do find in three models abrupt changes in the North Atlantic SPG in ocean variables which are clearly driven by the significant, but non-abrupt mixed layer depth decrease occurring there. Although that decrease was not itself classified as abrupt in two cases it is classified as a category B SNS under an SSP585 forcing, implying
250 a transition to a new (largely collapsed) state in the SSP585 simulation of that model. In GISS-E2-1-G this occurs for sea surface salinity (SSS) in SSP245 and SSP370, and for sea-surface temperature (SST) in SSP370 only; Figure 7. Since both SSS and SST decrease, the driver for the mixed layer decrease must come from SSS decreasing the surface density, only partly counteracted by the cooling that increases the surface density. This type of abrupt change occurring in CMIP6 models was recently described by Swingedouw et al. (2021), using different (and somewhat less stringent criteria). The SNS in GISS-E2-
255 1-G was classified as a false positive that in Swingedouw et al. (2021), in terms of atmospheric cooling, but here we clearly show that the model's surface temperature and salinity respond abruptly to the abrupt shoaling of its mixed layer (Figure 7).

The climatic impacts of such abrupt mixed layer collapses can be substantial (see also Sgubin et al. (2017)) but remain less than 1.5 °C in the GISS-E2-1-G model, smaller than events in models that were not classified as abrupt here. Similar mixed layer decrease-induced abrupt changes in ocean variables occur for GISS-E2-1-H and for CESM2-WACCM (SSS in SSP585).

260 3.5 State transition to extremely shallow Northern Hemisphere mixed layers, associated with similar transitions in salinity and ocean temperature (B)

While we do not find abrupt changes in mixed layer depth, we do agree that various models show significant transitions from deep convection in the SPG to a state of no deep convection. This becomes more evident when data after year 2100 is included in the analysis. In our analysis, 10 models are identified featuring a collapse in mixed layer depth in the Atlantic
265 SPG and/or Nordic Seas. These are ACCESS-CM2, ACCESS-ESM1-5, CESM2, CESM2-WACCM, GISS-E2-1-G, GISS-E2-2-G, HadGEM3-GC31-MM, MRI-ESM2-0, NorESM2-MM, and UKESM-0-LL. Swingedouw et al. (2021) discussed three of these models in their analysis (CESM2-WACCM, MRI-ESM2-0, and NorESM2-LM). Interestingly, these three events were exclusive to the SSP585 scenario. In our analysis the mixed layer collapse also occurs in more weakly forced scenarios. In

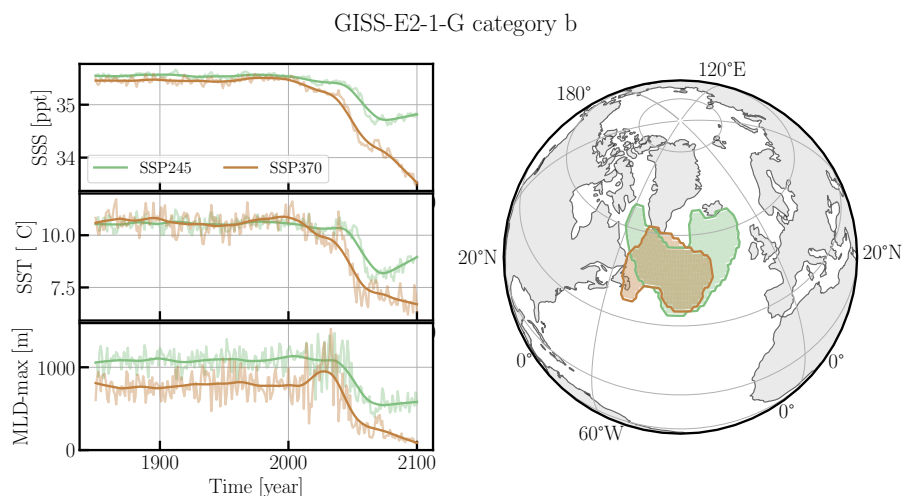


Figure 7. Category “b” for the GISS-E2-1-G model (SSP245: r2i1p5f1, SSP370: r4i1p5f1). The region SSP245 belongs to the SNS detected in SSS, while the SNS for the SSP370 region is detected in SST. See caption of Figure 4 for details.

CESM2 and MRI-ESM2-0, it also occurs in the SSP126, SSP245, and SSP370 scenarios; in CESM2-WACCM also in all
 270 scenarios but the SSP370 scenario was not run there. Curiously, in the GISS-E2-2-G model, the collapse occurs only in the
 SSP126 and SSP245 scenarios. These dramatic shifts in mixed layer depth are, due to our requirement that they occur over
 an area of at least 10^6 km^2 , more often occurring over larger areas than just the Labrador Sea; often over the whole SPG and
 parts of the Greenland, Iceland and/or Norwegian Sea as well. In the UKESM-0-LL the collapse occurs in the Nordic Seas
 and develops between years 2020 and 2060; in the MRI-ESM2-0 and GISS-E2-1-G the collapse also includes the mixed layer
 275 depth in Labrador and Irminger Seas. In the other models the collapse occurs in the Labrador and Irminger Seas only (e.g.
 Figure 8). This North Atlantic mixed layer collapse occurring during the early to mid 21st century and often already starting
 around 2020 is robust for all models showing a collapse. In Drijfhout et al. (2024a), the collapse is analysed for the much
 smaller deep convection area and for the maximum mixed layer (March) only, showing a far more abrupt signal with steepest
 decline around 2050. There, it is argued that the North Atlantic mixed layer collapse precedes the AMOC collapse, and that
 280 this appears to be the main cause for the AMOC winding down to extremely weak states.

It should be noted that these collapses can occur in all SSP scenarios with an onset that sometimes already starts at a
 1 °C warming level in the beginning of the 21st century, suggesting a strongly increased sensitivity in CMIP6 of mixed layer
 depth and deep convection to global warming levels compared to CMIP5. Given the spread in warming level for the SPG-
 and Nordic Seas-convection collapse to occur, it is unlikely whether global warming level is the right metric to measure its
 285 possible onset. As was already discussed in Drijfhout et al. (2015); Sgubin et al. (2017); Swingedouw et al. (2021), the onset
 of the collapse primarily occurs when the density stratification crosses a certain threshold, and this is more often caused by
 upper-layer freshening than by upper-layer warming, see also Drijfhout et al. (2024a).

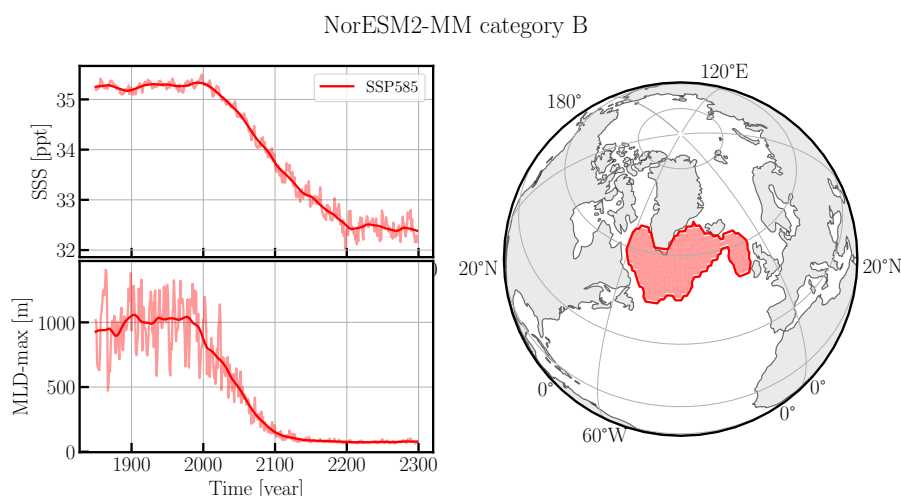


Figure 8. Category “B” for the NorESM2-MM model (r1i1p1f1). The region (left) belongs to the region of the SNS detected in MLD-max. In this model run, the SSS also showed an SNS, that extended further in the Baffin Bay and less far eastwards. For consistency, the left panels correspond to the region in the right panel. See caption of Figure 4 for details.

In most cases the mixed layer collapse is caused by a polar halocline, due to strong freshening of parts of the SPG. In all models the SPG freshens, especially at the surface, but in models in which the maximum mixed layer collapses in deep convection regions, this occurs abruptly and is associated with a transition from deep to shallow mixing. When looking to annual mean SSS in larger regions, the regions of maximum mixed layer weakening and SSS decrease no longer fully coincide. In NorESM2-MM the mixed layer weakening is strongest in the Labrador and Irminger Seas, while the maximum SSS decrease is somewhat shifted northward, including the Baffin Bay as well (where no deep mixing occurs). Other models that show large decreases in SSS in parts of the North Atlantic are CESM2 (Eastern SPG); CanESM5 (Labrador Sea and Baffin Bay); GISS-E2-1-H (Hudson Bay) and UKESM1-0-LL (Labrador Sea and Baffin Bay). However, in each case an SSS decrease over the deep mixing regions is a prerequisite for the convection collapse to occur. It is unclear without extensive further analyses to what extent direct freshwater forcing or reduced advection of salinity by a weakening AMOC through a Stommel feedback is dominant and whether the latter is triggered by reducing heat loss from the ocean to the atmosphere or whether forcing and feedback act in concordance, also see van Westen et al. (2024b) for more discussion on this topic. In some models, the mixed layer collapse is associated with a large state transition in SSS to much fresher surface waters. In ACCESS-CM2, CanESM5, NorESM-MM (Figure 8) and UKESM1-0-LL this occurs in the Baffin Bay and Labrador Sea with sometimes an extension into the Hudson Bay and along the Labrador Current. Notably, in CanESM5, the mixed layer collapse itself does not qualify as an SNS, but the large-scale freshening in this region does. In GISS-E2-1-H and MRI-ESM2-0 the same process occurs over the whole SPG and large parts of the Arctic. The freshening of the Arctic must be associated with the melt and year-round disappearance of nearly all sea-ice there. In CESM2, the large-scale freshening occurs in eastern SPG.

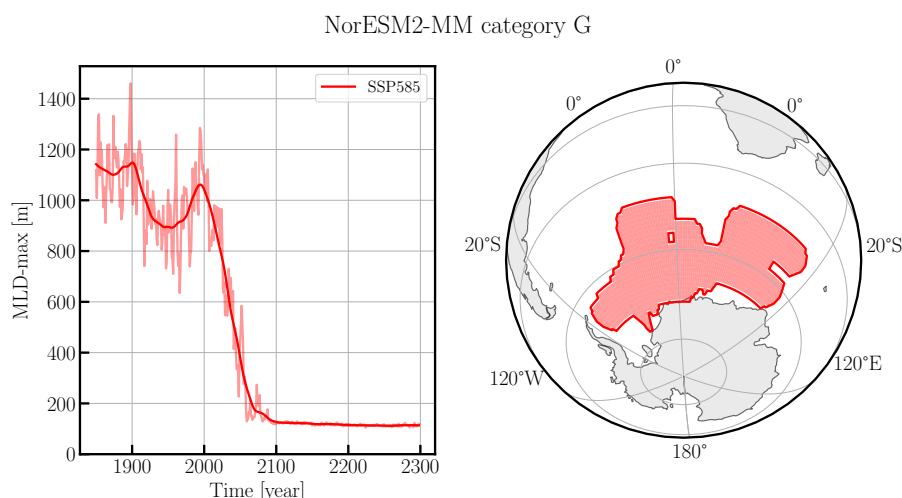


Figure 9. Category “G” for the NorESM2-MM model (rli1p1f1). See caption of Figure 4 for details.

3.6 Transition to extremely shallow Southern Hemisphere winter mixed layers (G)

Mixed layer collapses also occur in the Southern Hemisphere, but less often than in the Northern Hemisphere. We identified 5 such cases for different models (ACCESS-CM2, ACCESS-ESM1-5, CNRM-CM6-1, NorESM2-LM, NorESM2-MM). Most of these cases show a collapse in the Weddell Sea or just east of it in the Lazarev Sea. CNRM-CM6-1 shows a collapse in an atypical area: the Davis Sea in the Indian Ocean sector of the Southern Ocean. This site is not particularly known for deep convection. The other models show a mixed layer collapse in, or just east of the Weddell Sea. In ACCESS-ESM1-5, this occurs in the Lazarev Sea east of the Weddell Sea. In the other three models the Weddell Sea is the site where the mixed layer collapse occurs (Figure 8). As with the North Atlantic cases, these collapses all occur during the 21st century. Since open ocean convection in the Southern Ocean is a widespread feature of lower-resolution ocean and climate models, while in the observations, this type of deep convection is rare, and most of the Antarctic Bottom Water and its even denser precursors is formed on the Antarctic shelves, we do not assign much significance to these cases (Heuzé, 2020). The processes identified here, however, could be representative of the Weddell Polynya, where open ocean deep convection sometimes occurs, if it is opened (De Lavergne et al., 2014; Rheinländer et al., 2021; Mchedlishvili et al., 2022). Anthropogenic-driven shifts in the Amundsen Low might play a role in causing abrupt changes on the Antarctic shelves, basal melt of the West Antarctic Ice Sheet and possibly the Antarctic Slope Current (Thompson et al., 2018), open ocean sea-ice and deep mixing (Holland et al., 2019; Drijfhout et al., 2024b).

3.7 Transition to extremely weak AMOC states (D)

Given the widespread convection collapse in large parts of the northern North Atlantic in 10 models, it is unsurprising that an AMOC collapse also appears in seven of these and in two additional models. In the 3 runs in which the mixed layer collapsed,

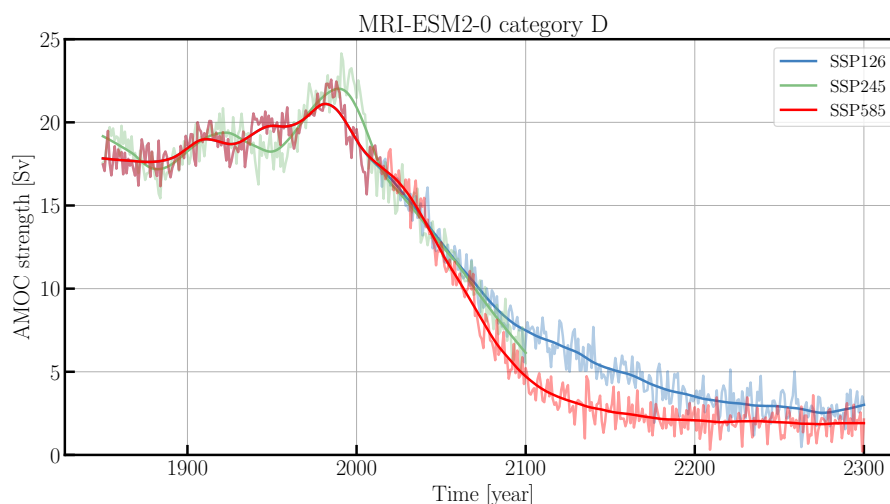


Figure 10. Category “D” for the MRI-ESM2-0 model (SSP126: r1i1p1f1, SSP245: r4i1p1f1, SSP585: r1i1p1f1). The yearly data is illustrated by the shaded lines while the solid lines depict the smoothed time series, where the smoothing is the same as in Figure 2.

325 but the AMOC did not, for one model (CESM2) the overturning streamfunction was not available, and for the other 2 models (GISS-E2-2-G and HadGEM3-GC31-MM) the respective runs stopped in year 2100, which is long enough to allow detection of a mixed layer depth collapse, but too short to detect an AMOC collapse. Note however that in GISS-E2-2-G the AMOC declined in the 21st century from ~ 25 to ~ 12 Sv and in HadGEM3-GC31-MM from ~ 18 to ~ 7 Sv, implying that, were these runs extended to 2300, they probably would have shown a collapsed AMOC, almost certainly for HadGEM3-GC31-MM. Because an AMOC collapse tends to develop more slowly than the SPG convection collapse, it most often identified in runs that were extended to year 2300. These include the previously discussed models showing an accompanying mixed layer depth collapse being the models ACCESS-CM2, ACCESS-ESM1-5, CESM2-WACCM, GISS-E2-1-G, MRI-ESM2-0, NorESM2-MM, and UKESM-0-LL. In all seven models the AMOC collapse occurs in extended SSP585 runs, but in CESM2-WACCM and MRI-ESM2-0 the collapse also occurs in the extended SSP126 runs. In addition, we identify an AMOC collapse

335 in the CanESM5 and MIROC-ES2L in their SSP585 runs. For these 2 models the mixed layer depth collapse was not observed. For MIROC-ES2L, the data was not available and in CanESM5 a mixed layer collapse can be seen but did not qualify as a category B SNS because all mixed layers in this model show a large decline. In MIROC-ES2L, the AMOC collapse proceeds rapidly enough to be detected in a run that ends in year 2100. The onset of AMOC decline occurs in these models between years 1980 and 2020, corresponding to global warming levels between 1.0 and 1.5 $^{\circ}\text{C}$, which is then completed between years

340 2150 and 2250 with an accelerated weakening until 2100 - 2150 and a slower approach to the new (quasi)-equilibrium. While a wind- and buoyancy-driven shallow overturning cell of ~ 3 Sv always remains in these runs, the 5 Sverdrup (Sv) boundary is crossed between 2100 and 2140 in most models. Only in the CESM-WACCM model in the SSP126 scenario the AMOC stabilizes around 5 Sv.

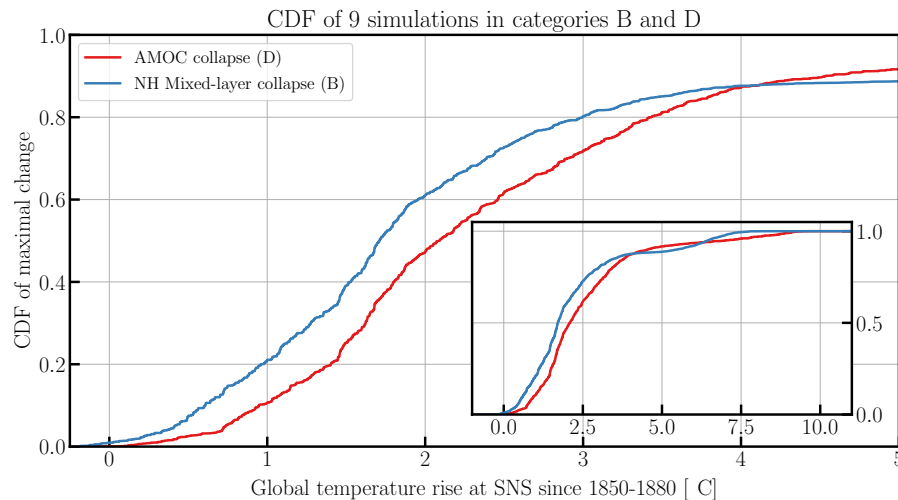


Figure 11. The change in category B SNS precedes the change in category D SNS. We show this using the cumulative distribution function (CDF) of the change being maximal before a global temperature rise for nine model runs that are in category B and in category D. We select the nine simulations (ACCESS-CM2, ACCESS-ESM1-5, CESM2-WACCM, GISS-E2-1-G, MRI-ESM2-0 (SSP126 and SSP585), NorESM2-MM (SSP126 and SSP585), and UKESM1-0-LL) that have the same ensemble-member in both categories B and D. The main panel shows that the collapse of the mixed layer depth occurs 0.3–0.4 °C before the collapse of the AMOC. The inset shows the CDF over the full temperature range. The approach to obtain this figure is similar to that of Figure 16 (see text for details subsection A3).

In the MRI-ESM2 model the AMOC declines to ~ 3 Sv in both SSP126 SSP245 and SSP585 scenarios, only a bit slower
 345 in the SSP126 and SSP245 scenarios. In this model the AMOC decline is similar in all scenarios until year 2050 (Figure 10);
 in CESM2-WACCM even until year 2080. The AMOC collapse under an SSP126 scenario is a novel finding. It underscores
 the increased AMOC-sensitivity in CMIP6 to warming (see also Jesse et al. (2024) and (Mecking and Drijfhout, 2023)). It
 also suggests that the AMOC collapse can possibly be identified with a real tipping point as it becomes independent of the
 forcing and may already be committed to collapse decades earlier in the 21st century. As for the convection collapse cases,
 350 we anticipate that the significant driver is density stratification in the northern North Atlantic and that freshening may play an
 equally large or even larger role than warming for the stratification to break deep convection when strong winter cooling occurs.
 This also implies that neglecting freshwater release from the melting Greenland Ice Sheet in present-day CMIP models may
 underestimate the likelihood of simulating an AMOC collapse and dampen its possible abruptness as, for instance, witnessed
 in the gradual increasing freshwater hosing experiment of van Westen et al. (2024a). The much earlier onset of SPG convection
 355 and AMOC collapse than previously estimated (Fox-Kemper et al., 2021; Armstrong McKay et al., 2022; Loriani et al., 2023)
 is illustrated by Figure 11.

3.8 Abrupt shift in the North Atlantic Current (c)

Many low-resolution coupled models feature a strong cold bias east of Newfoundland due to an overly zonal North Atlantic
 Current (NAC) (Moreno-Chamarro et al., 2021). Associated with this bias in the current pathway a cold anomaly appears in

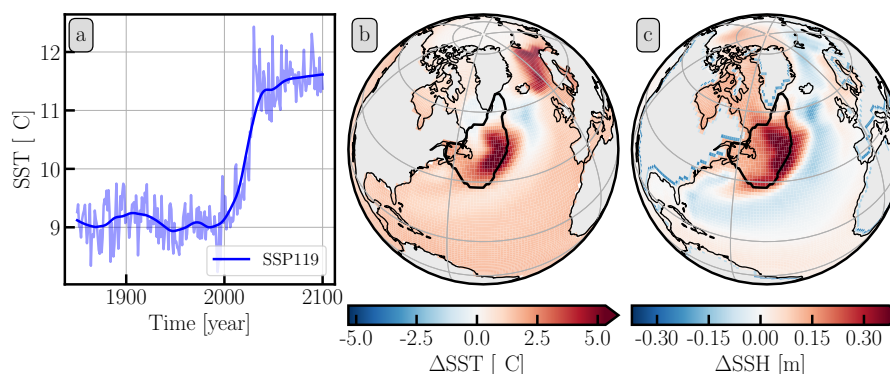


Figure 12. The time series of category “c” (panel a), together with the change in SST (panel b) and SSH (panel c) are shown for GISS-E2-1-H (r1i1p3f1). The change for SST and SSH is calculated between the averages for the 1850 – 1880 and 2070 – 2100 periods. The black outlined region in panels b and c illustrates the location of the SNS region. Since the global average SSH over time in GISS-E2-1-H does not equal zero (that would be the dynamical sea-level rise), we manually subtract the global average SSH from each year’s data. The yearly data in panel a are illustrated by the shaded lines while the solid lines depict the smoothed time series, where the smoothing is the same as in Figure 2.

360 sea-surface and surface atmospheric temperatures, which is often called the northwest corner bias. This bias is also present in the GISS-E2-1-H model, but surprisingly, NAC and surface temperatures feature an abrupt shift to a more northward pathway for the NAC through the central/eastern SPG, and subsequently warmer temperatures east of Newfoundland under the SSP119 scenario. The temperature change in the ocean is almost 3°C and in the surface atmosphere over 2°C , the upward heat flux doubles and sea surface height increases by almost half a meter. The change in SST is most abrupt, occurring within a decade
365 around 2030 (Figure 12). Why this change in NAC occurs most sharply in the SSP119 scenario in this model remains unclear, but it is remarkable that the bias can abruptly change in response to a modest increase in radiative forcing, much more than when that forcing becomes stronger in a higher-emission scenario. That the NAC can be steered by applying advanced forms of local flux correction was demonstrated by Drews et al. (2015), who argued that this also must be applied to the subsurface to adjust the flow field by modifying density and pressure gradients over a large vertical column. We hypothesize that in this
370 model, perhaps by chance, the temperature and salinity adjustment in response to an SSP119 forcing conspire to change the pathway of the NAC. The GISS-E2-1-H model suggests the NAC can feature abrupt pathway changes that resemble a tipping point, but whether such a tipping point exists in nature is unclear. Further investigation of this abrupt change, however, could be valuable in guiding bias reduction efforts in models with a northwest corner problem.

3.9 Transition to much increased Antarctic Circumpolar/Ross Gyre (H)

375 Three models show a very strong drop in sea surface height (SSH) south of the Antarctic Circumpolar Current (ACC) associated with an increase in ACC mass transport of approximately 50 % in the SSP585 scenario (CESM2-WACCM, MRI-ESM2-0, UKESM1-0-LL). This is most likely related to the ACC response to the intensification of the Southern Hemisphere westerlies (Bracegirdle et al., 2013). This response, however, is probably spurious, in the sense that higher-resolution models show a

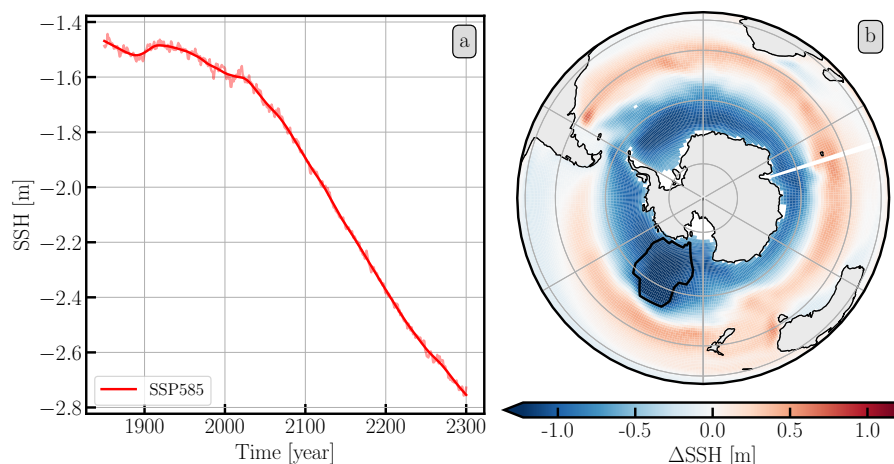


Figure 13. Time series (panel a) of category “H” in IPSL-CM6A-LR (r1i1p1f1) together with the change in SSH (panel b). The change of SSH is calculated between the averages for the 1850 – 1880 and 2270 – 2300 periods. See the caption of Figure 12 for further details.

much weaker ACC-sensitivity to winds, caused by what has been named “eddy saturation” (Munday et al., 2013), consisting of an intensification of the eddy field in response to increasing winds, rather than an increase in mean ACC transport. As a result, both SROCC (Meredith et al., 2019) and AR6 (Fox-Kemper et al., 2021) have assessed that the ACC is likely to remain only weakly sensitive to increasing winds. Moreover, such strong ACC response to winds may be enhanced by model bias explaining a large part of the spread in projections of CMIP5 models (Bracegirdle et al., 2013), which most likely also holds for CMIP6 models.

One model (IPSL-CM6A-LR) shows a very strong drop in SSH just east of the Ross Gyre in the SSP585 scenario, associated with an 80 % increase in its regional depression. This appears to be a sign of an eastward expansion of the Ross gyre, which also occurs in the UKESM1-0-LL (but less extreme than in IPSL-CM6A-LR), and was analysed by Gómez-Valdivia et al. (2023). They argued that sea-ice loss in the Amundsen-Bellingshausen sector enhances the wind stress curl on ocean water driving the eastward expansion of the Ross Gyre. This scenario was also described in a higher-resolution regional model of the region (Holland et al., 2019). Furthermore, the same process was already found to occur during the historical period (using an ensemble of high-resolution regional models forced with reanalysis data (Naughten et al., 2022)). As a result, this particular state transition is more credible than the projected increase in the ACC in some models.

IPSL-CM6A-LR also features a strong drop in SSH south of the ACC (Figure 13), but here the circumpolar drop in SSH is slightly too small to classify the entire region as a state transition. The other models (CESM2-WACCM, MRI-ESM2-0, UKESM1-0-LL) that do identify the entire circumpolar region as a state transition in SSH show a less pronounced drop in SSH in Ross Gyre than in IPSL-CM6A-LR. It is unclear whether the drop in SSH in the eastward extension of the Ross Gyre would classify as a state transition in a more realistic eddy-resolving model. In such a model, the ACC typically exhibits eddy saturation, and the circumpolar drop in SSH south of the ACC is either absent or remains modest. Nevertheless, the response of the Ross Gyre appears robust and is corroborated in forced high-resolution ocean-sea-ice models.

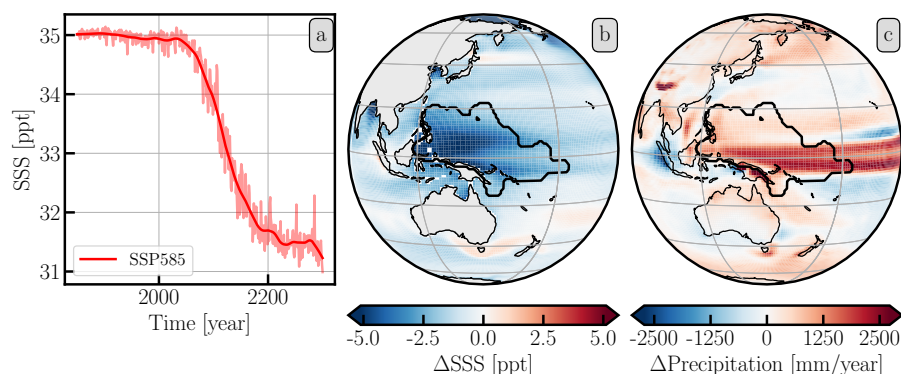


Figure 14. The time series (panel a) of category “E” in IPSL-CM6A-LR (r1i1p1f1) is shown together with the change in SSS (panel b) and precipitation (panel c). The change for SSS and precipitation is calculated between the averages for the 1850 – 1880 and 2270 – 2300 periods. See the caption of Figure 12 for further details.

3.10 Transition to new ITCZ state (E)

Large changes associated with a reorganization of the ITCZ are found in large-scale SSS transitions to much fresher surface waters in the western tropical Pacific in ACCESS-CM2, ACCESS-ESM1-5, CESM2-WACCM and IPSL-CM6A-LR. An example of this transition is given in Figure 14. These changes occur exclusively in the SSP585 scenario and are associated with model bias. Many low-resolution coupled models feature a double ITCZ, especially over the Pacific Ocean (Moreno-Chamarro et al., 2021). This is also the case in the IPSL-CM6A-LR model and while the bias does not disappear in the SSP585 scenario, the signal over the equator, especially in the west Pacific, decreases abruptly. This is associated with a strong increase in rainfall over the region and reduced evaporation, caused by the double ITCZ becoming less pronounced. This change in ITCZ pattern causes a drop in salinity in the Pacific across the equator and most notably north of it, which occurs most abruptly along the western Pacific equatorial zone in one member³ of IPSL-CM6A-LR (Figure 14). It is doubtful whether this change can be associated with a tipping point in the real world, as it originates from a strongly biased climate system. On the other hand, it is related to strong (positive) feedbacks between clouds, atmospheric convection and atmospheric/oceanic circulation that also work in Nature (Hwang and Frierson, 2013; Zhang et al., 2019).

3.11 State transition to much more humid climate over and in the Southern Ocean associated with strong intensification of the hydrological cycle (I)

A somewhat similar type of transition is an increase in freshwater flux in the Southern Ocean. This occurs in the CanESM5 model in the SSP585 scenario for the Amundsen-Bellingshausen sector (Figure 15) and for the wider Weddell gyre.

³The algorithm also detected the change in the r6i1p1f1 member, which runs only up to 2100. For this ensemble-member, this region fulfilled criterion ii, which would strictly speaking classify it as an abrupt shift. However, as the evolution is so similar to that observed in r1i1p1f1, we decided against discussing r6i1p1f1 separately as an abrupt change.

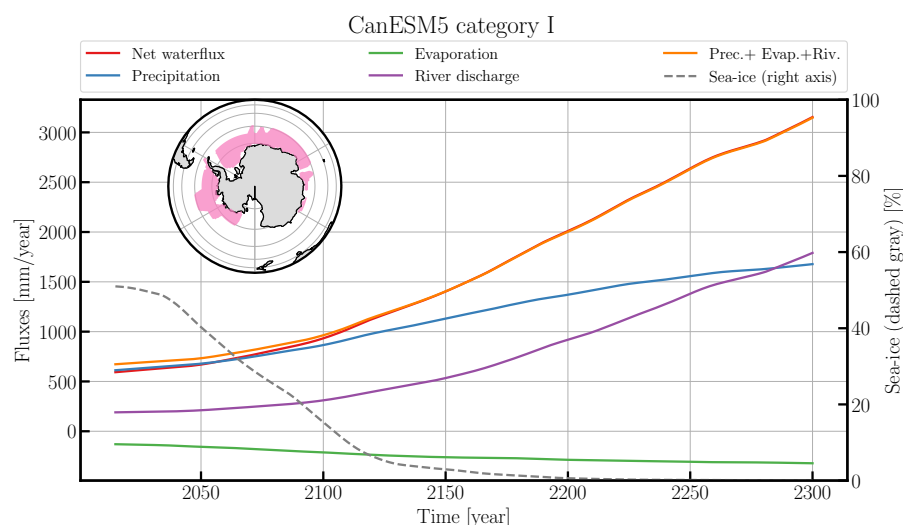


Figure 15. Case “I” for the CanESM5 model (r1i1p1f1) as found in the net water flux, split by precipitation, evaporation and river discharge (purple). By summing (Prec. + Evap. + Riv.) the contributions of precipitation, evaporation, and river discharge we are able to close the water budget in this region. The right axis additionally shows the sea-ice cover in this region. The inset shows the region of the category I case in the CanESM5 model, where the region of the SNS is illustrated as the pink shaded region.

Although sea-ice cover dramatically decreases over these two areas, the increase in net water flux from atmosphere to ocean is not related to this (Figure 15). It is shown that the increase in river run-off from the Antarctic continent (read snow melt and iceberg calving) plus precipitation (rain and snow) over the area (which also includes rain and snow over sea-ice) almost completely explains the increase in net water flux and when the increased evaporation (which acts as a negative contribution to this water flux) is included, the balance is closed. The reason for this large increase in water flux is thus the very strong increase in the hydrological cycle and transport of atmospheric water (vapor) from further north to the Southern Hemisphere subpolar areas, in particular the eastern Pacific and western Atlantic sectors. It should be noted that CanESM5 features one of the highest Equilibrium Climate Sensitivities of CMIP6 (5.64 (Zelinka et al., 2020)), and as a result the intensification of the hydrological cycle is particularly strong in this model.

4 Discussion

In this work, we have searched for SNS in CMIP6 data, focusing on ocean, sea-ice, and atmospheric variables. We identified 73 SNS that we grouped into 11 categories. Compared to Drijfhout et al. (2015), where 37 SNS were identified, this represents a surprisingly large increase. This is especially evident when considering that Drijfhout et al. (2015) investigated similar ocean, sea-ice, and atmospheric CMIP5 variables, as well as several land-use and carbon-cycle related variables. Furthermore, Drijfhout et al. (2015) also searched for bi-modal switches, and extended their search to SNS in pi-control simulations (where they isolated an additional 4 SNS). On the other hand, Drijfhout et al. (2015) included 37 models for 3 RCPs, while this work considers 54 models for 5 SSPs.



The method used here also made substantial changes to the approach discussed in Drijfhout et al. (2015). This allows for the
435 isolation of arbitrarily shaped regions, while the region-selection in Drijfhout et al. (2015) was performed manually in rough
 $5^\circ \times 5^\circ$ rectangular longitude-latitude boxes and strict selection was already implied by the expert making the region-selection.
In this work we instead rely on formal, stringent criteria and apply those to the arbitrarily shaped regions. Compared to the
method used in Drijfhout et al. (2015) our method has now become fully reproducible, as it no longer relies on expert judgment
of time series. The fact that this work uses highly optimized regions compared to the rectangular longitude-latitude boxes in
440 Drijfhout et al. (2015) is partially compensated by the increased area-threshold we use of 10^6 km^2 compared to $0.5 \times 10^6 \text{ km}^2$.

Especially the increased number of models that fulfil category A/a is a strikingly different compared to Drijfhout et al.
(2015), as discussed in subsection 3.1 and subsection 3.2, as well as the increased number of SNS categories D (subsec-
tion 3.7), especially in the low emission scenarios. The related category B/b also saw a significant increase (subsection 3.4 and
subsection 3.5).

445 In section 3, we discussed each of the 11 categories of SNS one by one. To see how often SNS occur in the available data,
we first calculated the number of simulations that reach a given global warming level (since 1850-1880). To emphasize the
contributions of the different SSPs, we considered each SSP for each model separately. That way, we have roughly 200 model-
SSP combinations. Next, we needed to obtain the period in which each shift occurs. This is not always easily identifiable, for
example panel iii in Figure 2 shows a sharp decline around year 2035, but also in year 2055, one might therefore argue that the
450 SNS occurs at either of these years (and the temperatures associated with these years) or at a time in between these years. To
overcome this ambiguity, we used a flexible window w of 20-50 years to find the years (and the temperatures associated with
them) at which the difference in w years in the w -year running mean is maximal, also see subsection A3 for more information.
The window w should be long enough to prevent measuring short term fluctuations as those apparent in panel v in Figure 2,
where before 1900 there are large, decadal time-scale changes (while the real change of interest evolves slowly in 2000-2050).
455 The same window, on the other hand, should not be so long that it will span the entire scenario run duration since then all global
warming temperatures will be associated with the SNS (such as Figure 2 panel i, which, using such a long window, always
occurs in 2050). The flexible window w of 20-50 years strikes a balance between these two opposing interests and gives a PDF
for the timing (and temperature) of maximum change.

We then calculate the frequency at which temperature the SNS occur by summing the PDFs of all SNS and dividing that
460 by the number of models that reach that global warming level. This leads to Figure 16 where the bottom shows the number
of available simulations for each temperature rise, while the top panel shows the frequency of SNS at each warming level.
We normalize this distribution so that each change is once accounted for (even if it is observed in more than one variable).
Additionally, models may have more than one ensemble-member, if this is the case, each of their temperature distributions is
divided by the total number of ensemble-members. The top panel therefore shows (as a function of global temperature rise



Frequency of SNS-events as function of warming level

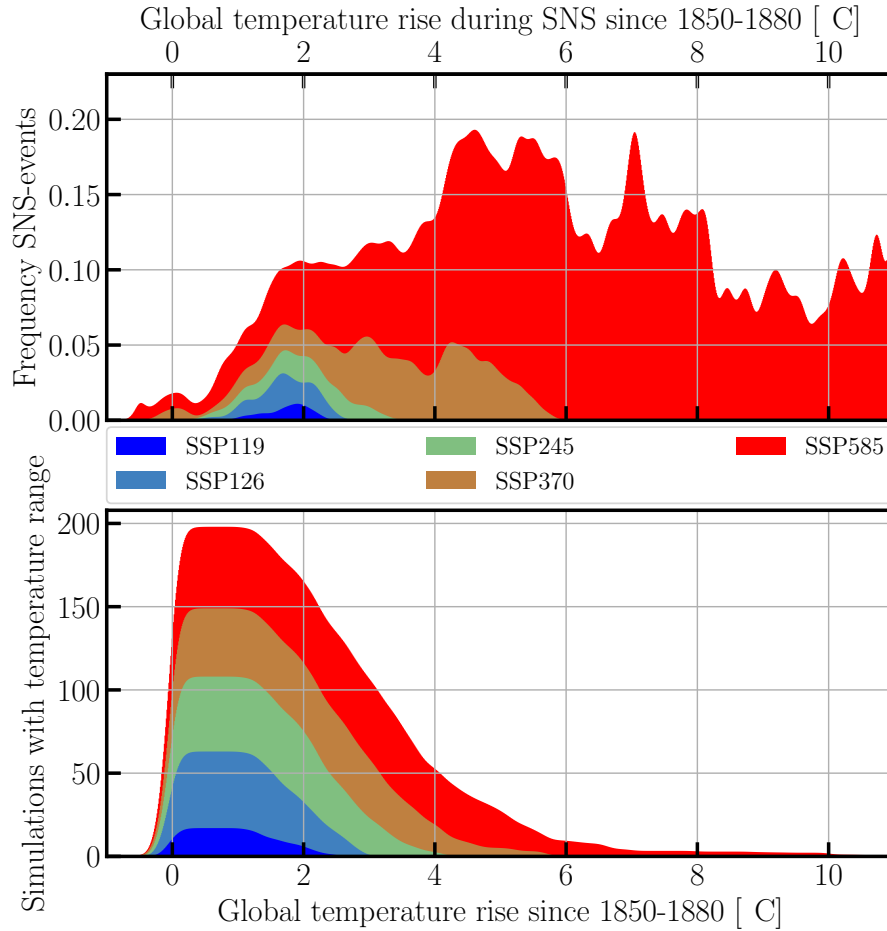


Figure 16. Frequency of SNS (top) as a fraction of the number of available simulations that reach such a temperature range (bottom). The frequency of a shift is calculated by dividing the summed fractional probability of an SNS to occur in a temperature interval, divided by the number of available simulations that cover that interval (see text for details). The data is smoothed using a Gaussian convolution with a standard deviation of 0.1 °C. The temperature scale (x-axis) is limited to 11 °C as motivated in the text.

465 ΔT):

$$\text{Freq.}(\Delta T) = \frac{\sum_{\text{SNS}} \sum_i^{n_{\text{variables}}} \frac{1}{n_{\text{variables}}} \sum_j^{n_{\text{ensemble}}} \frac{1}{n_{\text{ensemble}}} \cdot \text{PDF}_{i,j}(\Delta T)}{\sum_{\text{model, SSP}} \sum_j^{n_{\text{ensemble}}} \frac{1}{n_{\text{ensemble}}} \text{simulation at } \Delta T}. \quad (1)$$

In Figure 16, we see a steep increase in the frequency of SNS between 0 and 2 °C, followed by a relative flattening between 2 and 4 °C. After 4 °C the frequency peaks, while the statistics quickly drop (bottom panel) and after 6 °C, the top panel starts



to suffer from limited statistics. We should emphasize that Figure 16 illustrates the warming level at which the changes in the
470 SNS are maximal, meaning that the initialization of the SNS always precedes this time. If a tipping point is associated to the SNS, it is passed *before* the temperature noted here, when the transition to the new state is occurring.

We limit Figure 16 to 11 °C global warming level. Only five ensemble-members reach temperatures higher than this value (ACCESS-CM2 r1i1p1f1, CESM2-WACCM r1i1p1f1, CanESM5 r1i1p1f1, EC-Earth3-Veg r13i1p1f1, IPSL-CM6A-LR r1i1p1f1, UKESM1-0-LL r4i1p1f2) all of which are in the extended (beyond year 2100) SSP585 scenarios, most of which
475 will feature a high probability of an SNS in the remaining temperature range. The small, unexpected bump near 0.5 °C warming is mostly an artifact by the fact that (despite the method explained in subsection A3) it is an artifact of the large maximum window size (50-years) that includes up to 25 years before (or after) the year of maximum change, combined with the very few simulations (bottom panel) that pass this temperature range.

We should note that the extended model runs (beyond the year 2100) are disproportionately represented in the SNS. The
480 number of extended models (each normalized by the number of ensemble-members available to that model) compared to the total number of available models clearly illustrates this overrepresentation. The number of normalized extended models / number of available models is: 0.3/17 (2.0 %) for SSP119, 4.5/46 (10 %) for SSP126, 1.6/45 (3.6 %) for SSP245, 0.0/41 (0.0 %) for SSP370, 3.0/49 (6.2 %) for SSP585. The relative frequency of extended runs in those models that show an SNS is much higher: 0.0/2 (0.0 %) for SSP119, 5.0/10 (50 %) for SSP126, 1.8/10 (18 %) for SSP245, 1.0/16 (6.3 %) for SSP370, 7.0/26
485 (27 %) for SSP585. The larger availability of extended runs compared to Drijfhout et al. (2015) is one additional reason why the frequency of SNS appears higher in our analysis.

In Figure 17 we illustrate the CDF of the SNS occurring as a function of a global temperature rise. We see that the state transitions (uppercase SNS categories) generally occur at later timescales compared to the abrupt shifts. There are several reasons for this difference between the categories. As seen in e.g. subsection 3.1 and subsection 3.2, the change in sea-ice is
490 sometimes observed as abrupt in the low-emission scenarios, while it is seen as a state transition in the high emission scenario where the disappearance of sea-ice is complete (see e.g. #6 and #27 in Table A3). Additionally, many state transitions are observed in the extended datasets. From Figure 16, we can infer the read of the temperature at which, for each category, the change in the SNS is maximal, being A $3.7^{+1.4}_{-1.2}$ °C, a $1.7^{+0.6}_{-0.4}$ °C, B $1.9^{+3.7}_{-0.7}$ °C, b $2.9^{+1.2}_{-0.7}$ °C, c $1.6^{+0.2}_{-0.5}$ °C, D $2.1^{+1.8}_{-1.0}$ °C, E $6.6^{+1.1}_{-1.5}$ °C, f $2.5^{+0.7}_{-0.5}$ °C, G $1.3^{+0.6}_{-0.6}$ °C, H $8.6^{+2.1}_{-2.2}$ °C, and I $14.1^{+1.8}_{-1.1}$ °C where the errors are the 68 % confidence interval.

It is impossible to compare our results on a one-by-one basis with those obtained in Terpstra et al. (2024), as the latter (partly)
495 focus on other variables, but more importantly, another scenario, namely the 1ptCO2 scenario, which starts in the preindustrial and increases every year with 1% its CO₂ concentration until the preindustrial value is doubled. What is immediately apparent, is that our and their approach both lead to the conclusion that in CMIP6 thresholds for abrupt shifts/SNS are earlier passed and at lower temperatures for all variables that we both analysed.

500 In this work, we have only focused on ocean, sea-ice, and atmospheric variables. A logical next step would be the assessment of carbon-cycle and related CMIP6 variables, as also Drijfhout et al. (2015) found a substantial number of SNS in this regime.

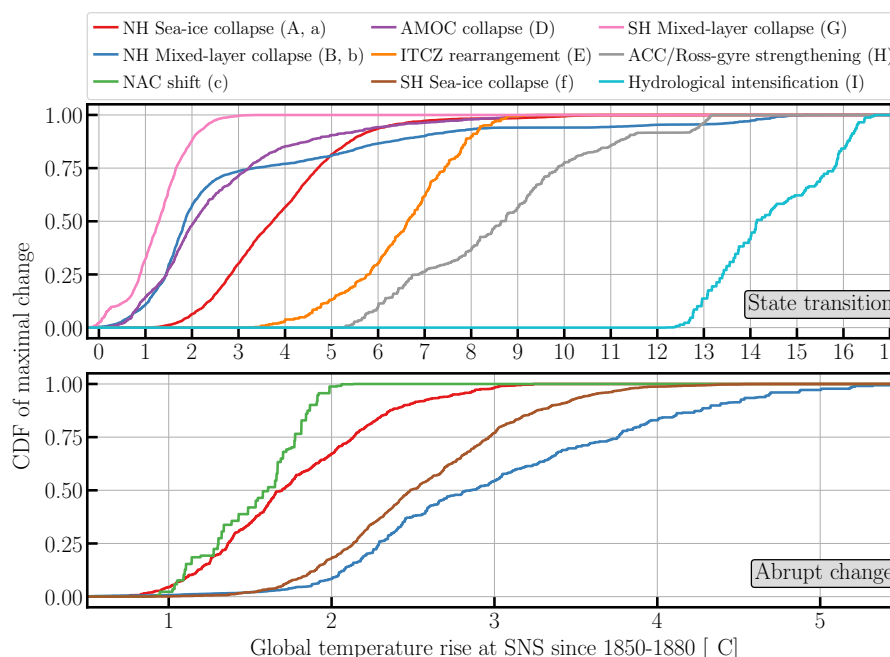


Figure 17. Conditional CDF for each category be maximally changing at a certain global warming level. The top panel gives the CDF for the state transitions (uppercase) categories while the bottom panel gives the CDF of the abrupt change SNS (lowercase) categories.

5 Conclusions

We have searched for SNS in CMIP6 data, with a focus on ocean, sea-ice, and atmospheric variables. We aimed to identify both abrupt changes over a decadal timescale and more gradual state transitions too large to be explained by increasing forcing only. We isolated 73 SNS that we categorized in 11 categories, which we each discussed. A large number 45% of SNS is attributed to sea-ice loss (categories A, a and f) relates to sea-ice cover, 29% to mixed layer depth (categories B, b and G), 19% to ocean currents (categories c, D and H), and 7% to atmospheric systems like the Intertropical Convergence Zone (categories E and I). The number of SNS steeply increases between global warming levels below 2 °C, stays at that level between 2 – 4 °C before rising further until around 6 °C, few models reach such high global warming levels. In general, the CMIP6 data contain various SNS that occur at lower temperature increase and earlier in time than estimated in previous assessments of SNS (abrupt changes) and tipping points, pointing to a increased sensitivity of the newest generation of climate models to anthropogenic forcing and an increased risk to strong nonlinear surprises. This finding signifies a strong warning to limit further future global warming as much as possible.



Appendix A: Appendix

515 A1 Formal criteria

Below we give the six criteria and their respective thresholds. The criteria were designed to isolate regions with spatially averaged time series that are extreme for the available CMIP6 data. Criteria i and ii are specifically designed to select regimes that feature a single abrupt change. These two criteria are general purpose and are applied to all CMIP6 variables in Table A1. Criteria iii-vi are instead formalized to select large-scale state transitions, which occur on longer timescales. Criteria iii-v are
520 for specific variables, while criterion vi is general purpose.

The criteria use slightly different metrics to achieve these aims. Below, we discuss the criteria one by one. Most metrics are related, e.g. the abrupt criteria (i and ii) use a maximum jump in 10 years in the time series in places where the state transition (criterion vi) uses the difference between the start and end of the time series. The selection of each threshold in the criteria below was an iterative process and based on careful selection by the authors. They are therefore subjective, and while criteria i,
525 ii and vi are designed to be general purpose, CMIP6 variables that were not investigated in this work may require better suited thresholds or optimized criteria.

A1.1 Criterion i

Criterion i is designed to select abrupt changes. To this end we calculate the spatially averaged time series (below, we will simply call this the time series) of an isolated variable (Figure 1). As we are interested in large changes in the time series, we
530 calculate the maximum jump (MJ) in a 10-year window, after smoothing the time series with a 10-year running mean. We want the maximum jump to be large with respect to the pi-control dataset and the average variability in the scenario dataset. To this end, we calculate the standard deviation of the 10-year running mean of the detrended time series of the pi-control dataset within the region, which we call σ_{piC} . We require that the jump seen in the scenario is at least $4.5 \times \sigma_{\text{piC}}$ as in the first line of Equation A1.

535 Additionally, we calculate the average standard deviation of all cells, based on their individual 10-year running mean of the detrended values. This gives us a measure of the average global variability in the pi-control. However, since the tropical latitudes have different average standard deviations, we only take the average over grid cells within the $23.5^\circ\text{S} : 23.5^\circ\text{N}$ band if 50 % of the grid cells of the selected region are in that latitude range. In case the selected region has less than 50 % in the $23.5^\circ\text{S} : 23.5^\circ\text{N}$ -band, we instead take the average over grid cells that are outside this band. We call this average standard-
540 deviation of the pi-control dataset $\bar{\sigma}_{\text{piC trop}}$. We require that MJ is extreme, compared to the average variability in that zone (either tropics or outside of the tropics) by imposing $MJ/\bar{\sigma}_{\text{piC trop}} > 10$ (second line of Equation A1).

Similar to $\bar{\sigma}_{\text{piC trop}}$, we also require that the MJ is extreme with respect to the average standard-deviation of the 10-year running mean of the detrended time series in a large-scale zone (tropics or outside tropics). Completely analogous to $\bar{\sigma}_{\text{piC trop}}$, we call this average $\bar{\sigma}_{\text{trop}}$ require that it is $5 \times$ smaller than MJ .

545 Furthermore, we require that the (un-smoothed, yearly) time series is not unimodal, but bi- or multimodal by applying the dip test for unimodality (Hartigan and Hartigan, 1985) and requiring that its value is below 1 %.



Finally, we select time series that show one clearly identifiable jump. We compare the largest jump (MJ) to the second largest jump of the same sign (that is at least 10 years removed from MJ). We call the ratio between these two jumps $J2$. As some time series have both increasing and decreasing jumps, we also explicitly calculate the largest jump that has the opposite sign from the largest jump anywhere in the time series. The ratio between these jumps we similarly call $J2_{\min}$.

Together, the thresholds in Equation A1 select time series with single, abrupt (in the timescale of 10-year) jumps in the time series that are unique for this region, as well as large when compared to the standard deviation of either averages of the pi-control or scenario datasets. The abruptness should cause a detectable bi/multi-modality to pass the Diptest. The full criterion reads:

$$\begin{aligned}
 & MJ/\sigma_{\text{PiC}} > 4.5 \wedge \\
 & MJ/\bar{\sigma}_{\text{PiC trop}} > 10 \wedge \\
 & MJ/\bar{\sigma}_{\text{trop}} > 5 \wedge \\
 & p_{\text{dip}} < 1\% \wedge \\
 & \min(J2, J2_{\min}) > 3.0 \wedge \\
 & \max(J2, J2_{\min}) > 4.5.
 \end{aligned} \tag{A1}$$

A1.2 Criterion ii

Criterion ii, similar to i, aims to detect abrupt changes. Criterion i often fails to identify abrupt changes when they occur at the end (or, theoretically, start) of the time series. When this occurs, a second state is not sufficiently sampled to pass the Diptest. By dropping the Diptest and increasing the requirement on the $J2$ and $J2_{\min}$ parameters, we are able to select this type of time series that fail criterion i. This leads to:

$$\begin{aligned}
 & MJ/\sigma_{\text{PiC}} > 4.5 \wedge \\
 & \min(J2, J2_{\min}) > 4.5 \wedge \\
 & MJ/\bar{\sigma}_{\text{trop}} > 5 \wedge \\
 & MJ/\bar{\sigma}_{\text{PiC trop}} > 10.
 \end{aligned} \tag{A2}$$

A1.3 Criterion iii

Criterion iii aims to select (almost) complete disappearance of sea-ice in a large-scale area. For an arbitrary region, this could easily be achieved, as a peripheral region of sea-ice may melt in a warming climate (e.g. starting from 50 % sea-ice cover ending with 0 %). Therefore, we require the regions to be at least $5 \times 10^6 \text{ km}^2$. Additionally, we require that the disappearance is at least 95 % of the maximal value in an area that is at least as large. We compute the maximal average in a connected area



575 (if it is of the same size) with the maximal sea-ice values. The ratio between the start and end time of the region of interest and this maximum value is what we call $ES_{S.I.}$, which should exceed 95 %:

$$\begin{aligned} \text{variable} &\in \{\text{siconc}, \text{siconca}\} \wedge \\ ES_{S.I.} &> 95\%. \end{aligned} \quad (\text{A3})$$

A1.4 Criterion iv

580 Criterion iv is similar to criterion iii and focuses on a large percentage drop in the time series. This criterion applies only to msftyz, msftmz, and it uses the workflow as described in (Drijfhout et al., 2024a) to analyze this data format. We calculate the decline between the maximum in the 10-year running mean ($\max(v_{\text{rm } 10}(t))$) and the last value in the 10-year running mean ($v_{\text{rm } 10}(t = t_{\text{end}})$), which we call $ME = \max(v_{\text{rm } 10}(t)) - v_{\text{rm } 10}(t = t_{\text{end}})$. We require that there is a loss of at least 70 % of the maximal value, as in the equation below:

$$\begin{aligned} 585 \quad \text{variable} &\in \{\text{msftyz}, \text{msftmz}\} \wedge \\ ME / \max(v_{\text{rm } 10}(t)) &> 70\%. \end{aligned} \quad (\text{A4})$$

A1.5 Criterion v

Criterion v is meant to isolate regions of dramatic and persistent loss of mixed layer depth. We utilize a longer running mean of 50 years since the mixed layer depth often shows large inter-annual variability. We require, analogous to criterion iv, that
590 the change of the 50-year running mean of the time series since the maximum is 90 % of that maximum. Additionally, we use $\sigma_{\text{PiC rm } 50}$ to filter out regions that also have large variability in the pi-control dataset (similar to criteria i and ii). Finally, we also use $ME_{\text{trop rm } 50}$, which is the difference between the maximum and end of the spatially averaged time series in the tropics/outside the tropics. With this last metric, we also filter out regions that are showing large declines when considering only that region but are not standing out significantly when considering a large zonal average. Combining these metrics leads
595 to:

$$\begin{aligned} \text{variable} &= \text{mlotst-max} \wedge \\ ME_{\text{rm } 50} / ME_{\text{trop rm } 50} &> 15 \wedge \\ ME_{\text{rm } 50} / \sigma_{\text{PiC rm } 50} &> 15 \wedge \\ ME_{\text{rm } 50} / \max(v_{\text{rm } 50}(t)) &> 90\%. \end{aligned} \quad (\text{A5})$$



600 A1.6 Criterion vi

Criterion vi is applied to variables not yet covered by criteria iii-iv. As a general-purpose search for state transitions, it uses the difference between start and end of the time series (SE), which has to be extreme compared to certain metrics. We compare SE to $\sigma_{\text{PiC trop}}$ and σ_{PiC} which have been discussed above. Similar to $ME_{\text{rm } 50}/ME_{\text{trop rm } 50}$ (criterion v), we also here formulate a requirement on SE/SE_{trop} (although in contrast to mlotst-max, this value may be negative, so an absolute value is required).
605 Finally, we filter out time series with a large decadal variability. We use the standard-deviation of the difference in the 50 and 10 year running mean ($\text{std}(v_{\text{rm } 50}(t) - v_{\text{rm } 10}(t))$) and require that SE is large with respect to this number. Combined, this leads to the following requirement:

$$\begin{aligned} & \text{variable} \notin \{\text{siconc}, \text{siconca}, \text{msftyz}, \text{msftmz}, \text{mlotst-max}\} \wedge \\ & SE/\sigma_{\text{PiC}} > 50 \wedge \\ 610 \quad & SE/\text{std}(v_{\text{rm } 50}(t) - v_{\text{rm } 10}(t)) > 40 \wedge \\ & SE/\bar{\sigma}_{\text{PiC trop}} > 60 \wedge \\ & \text{abs}(SE/SE_{\text{trop}}) > 4. \end{aligned} \tag{A6}$$

A2 Variables and available data

We used CMIP6 variables in this work which we list, together with their short notations, in Table A1.

615 In Table A2 we list all the available data used for making this catalogue. The data are limited to those available at the time of writing, sets where a matching pi-control, historical and scenario run is complete and available.

A3 Temperature at maximal change of an SNS

In section 4 and Figure 11 we discuss the PDF/CDF (Cumulative Density Function) of shifts occurring at a certain global temperature rise. Figure A1 illustrates the method for obtaining the PDF/CDF for an example time series (SNS #6 of Table A3).

620 To do this, we analyze the spatially averaged time series of an SNS, as shown in panel a. First, we determine the time at which the change occurs. We find the largest change in a w -year window in the time series that we smooth by a w -year running mean. We assign an equal probability to all years within that w -year window. We repeat this for w from 20 to 50 year, as SNS typically evolve on such timescales. This results in the PDF and CDF in panel b of Figure A1.

To account for this, we take all temperatures in a window (w) into account around the year where the w -year difference in the time series is maximal (a w -year running mean). Each temperature within that time region is treated with equal probability. We repeat this for w from 20 to 50 year to build a temperature distribution at which the change is maximal. Panel b shows the PDF and CDF of the timing at which the change is maximal. By weighing the temperature change since 1850-1880 (panel c) with the PDF from panel b, we are able to build a PDF of the shift occurring at a certain temperature rise (panel d).



CMIP6 variable	Short notation	CMIP6 description
hfds	Heatflux	Downward Heat Flux at the Sea Water Surface
mldst	MLD	Ocean Mixed Layer Thickness Defined by Sigma-T
mldst_max	MLD-max	Yearly maximum of mldst
msftbarot	Barotropic Streamfunction	Ocean Barotropic Mass Streamfunction
msftmz	AMOC strength	Ocean Meridional Overturning Mass Streamfunction
msftyz	AMOC strength	Ocean Y Overturning Mass Streamfunction
siconc	Sea-ice, sic	Sea-Ice Area Percentage
siconca	Sea-ice, sic	Sea-Ice Area Percentage (Atmospheric Grid)
sos	SSS	Sea Surface Salinity
tas	TAS	Near-Surface Air Temperature
tos	SST	Sea Surface Temperature
wfo	Net waterflux	Water Flux into Sea Water
zos	SSH	Sea Surface Height Above Geoid

Table A1. The CMIP6 variables along with their sort notation (used throughout this paper) as well as the CMIP6 description. The variables msftyz and msftmz have a different data-format than the other CMIP6 variables, which are surface variables. The handling of msftyz and msftmz is therefore different as discussed in section 2 and only criterion iv is applied to this data.

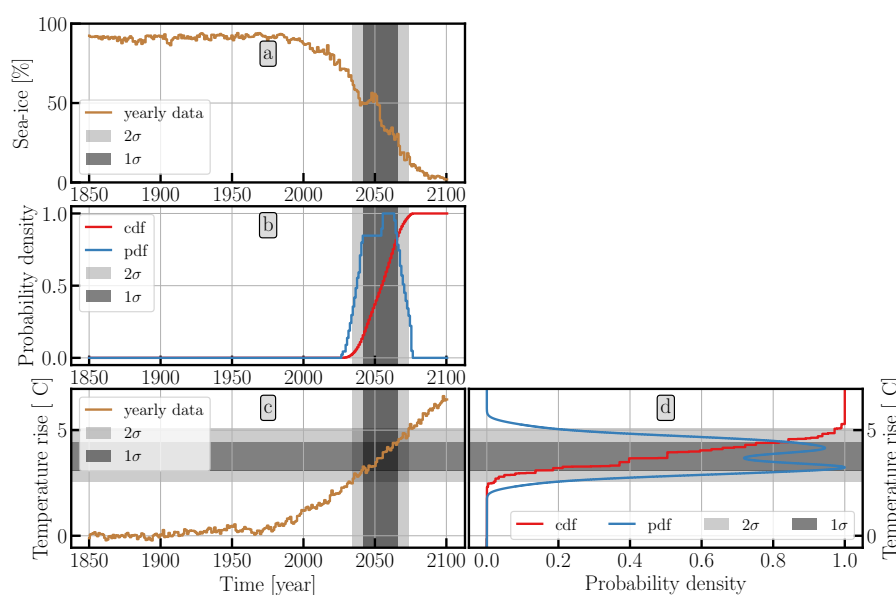


Figure A1. Method of obtaining the global temperature rise at shift for an SNS. We analyze the yearly data of panel a (see text for details) to determine when the change is maximal. The resulting CDF and PDF are shown in panel b. Based on the CDF in panel b, we draw the vertical 1σ and 2σ probability intervals. In panel c, we add the global temperature rise relative to the 1850-1880 average. By weighing the temperature rise values with the PDF of panel B we can calculate panel d, where we show the CDF and the PDF of the shift to occur at a certain temperature rise. The PDF in panel d is smoothed by a Gaussian with a standard deviation of 0.2°C for illustration purposes. The horizontal 1σ and 2σ probability intervals are based on the CDF of panel d.



Table A2. Number of ensemble-members per model, per variable, per SSP. For each variable we list the five SSPs separated by commas such that e.g. “hfdIs: 0, 0, 0, 0, 0” indicates 0×SSP119, 0×SSP126, 1×SSP245, 2×SSP370, 1×SSP585 for hfdIs.

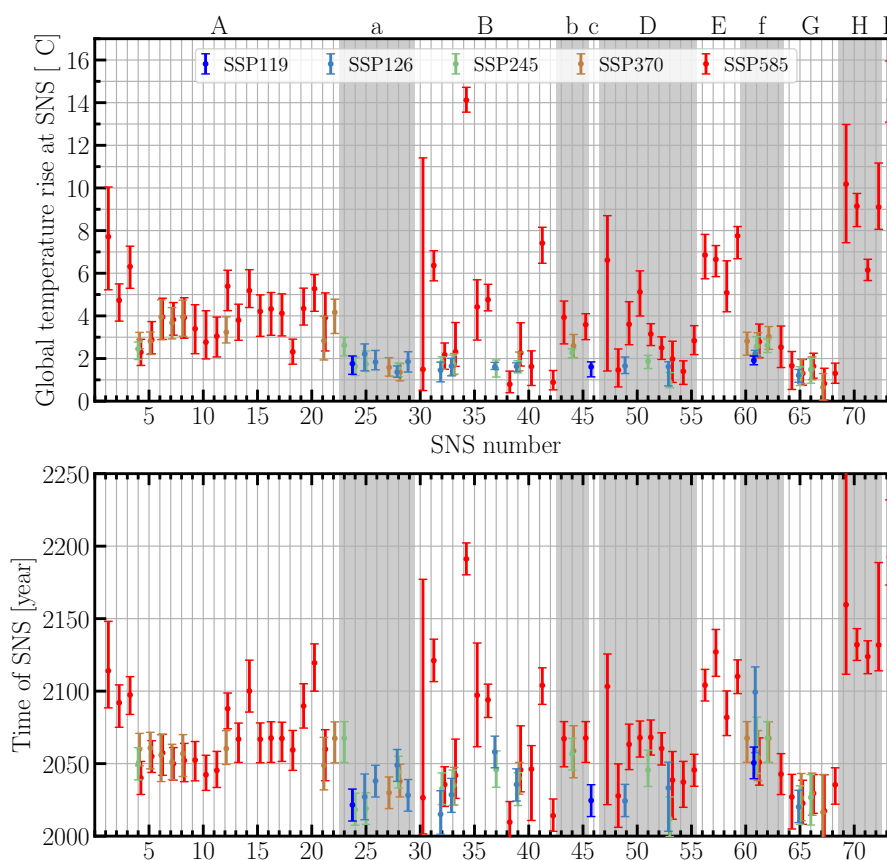


Figure A2. Median global temperature rise at SNS for all 73 SNS. The error bars indicate the 1σ confidence interval. Per case, the contributions of the SSPs are split (and slightly shifted horizontally for illustration purposes). The letters (top) denote the category to which the SNS belong and the categories are also illustrated using alternating background shades.

A4 SNS

630 In Table A3 we include each of the 73 SNS. As apparent from the table, one SNS is the occurrence of an event of one of the 11 SNS categories in a model. One SNS can be manifested in multiple variables or SSPs, as long as their associated regions are spatially overlapping. Some categories span a large spatial region, for this reason one model can result in more than one SNS per category, for example #8 and #9 in Table A3. In table Table A4 we additionally list the number of ensemble-members that pass for each variable, for each case listed in Table A3. The format is similar to Table A2, where we list each passing ensemble-member per passing case, per variable, per SSP. When no passing member of a given SSP occurs, we denote this with “-”. For the SSPs where there is at least one ensemble-member, we also list the total number of ensemble-members for that SSP (which is also listed in Table A2). For example, “siconc: -, -, -, -, 1/10” indicates that this SNS did not manifest in SSP119, SSP126, SSP245, or SSP370, only in SSP585 we did observe the SNS in one member out of ten for siconc.



640 The global temperature rise at the time of the SNS within a given category may vary significantly per model (as we have seen in Figure 17). We can instead also calculate the CDF per SNS, as shown in Figure A2. Each of the 73 cases is plotted separately, and split per SSP. As expected from Figure A1, the 1σ -confidence interval in Figure A2 can be skewed, depending on the evolution of the time series and global temperature rise within the model.

Figure A3 illustrates the first ensemble-member per case, where we show each variable per SNS category in a single panel.

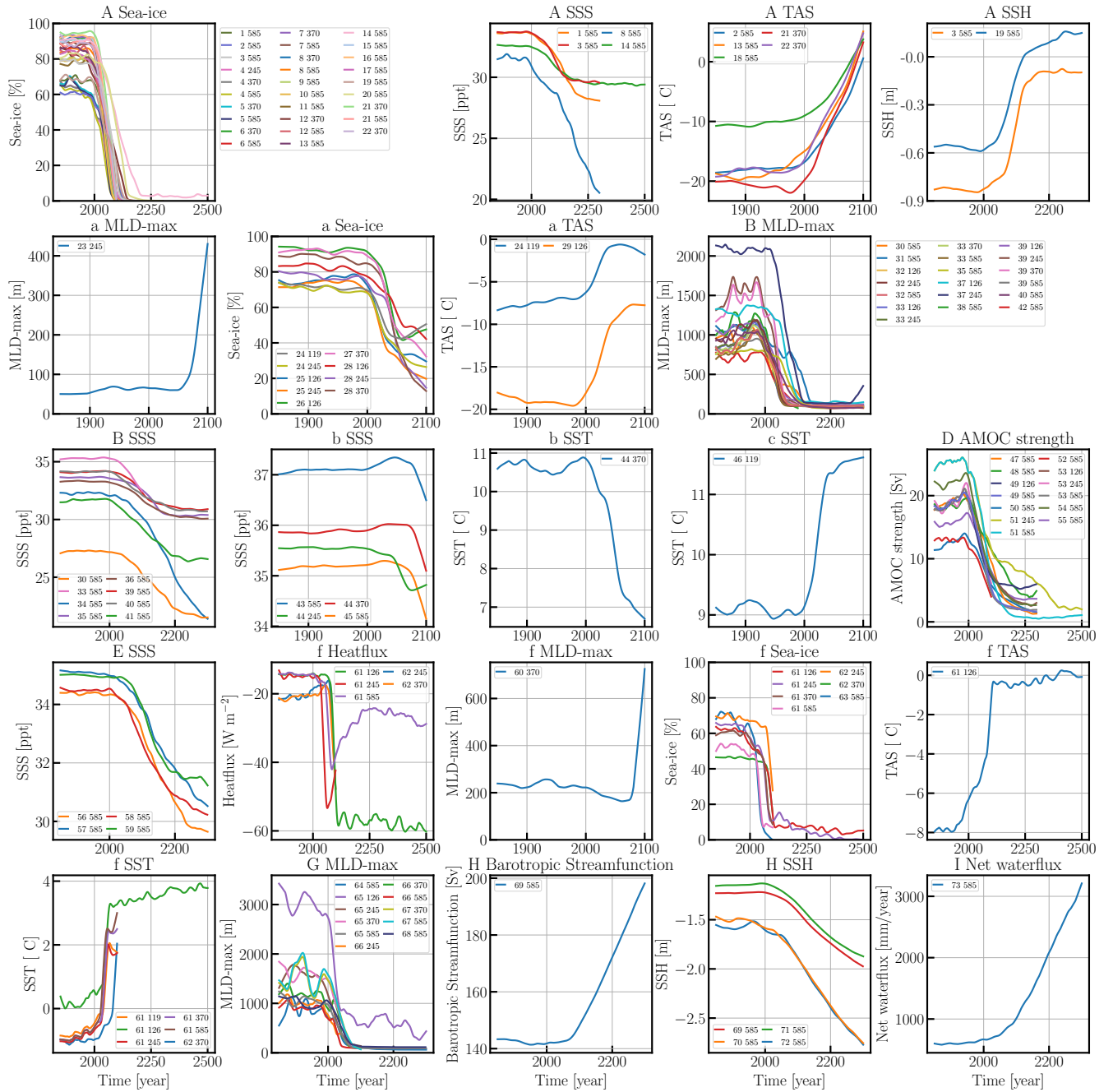


Figure A3. Time series of the first ensemble-member of each SNS case from Table A3. The time series are split per SNS category, and per variable within the SNS category, represented by the title of each panel. The legend labels refer to the SNS number in Table A3 and the SSP (119, 126, 245, 370 or 585). For illustration purposes, the time series are smoothed using a Lowess filter with a window of 40 year.



#	Cat.	Model	SSP	Crit	Vars	Region
1	A	ACCESS-CM2	585	iii, vi	siconc, sos	Arctic Ocean
2	A	ACCESS-ESM1-5	585	iii, vi	siconc, tas	Arctic Ocean
3	A	CESM2-WACCM	585	iii, vi	siconc, sos, zos	Arctic Ocean
4	A	CMCC-CM2-SR5	245, 370, 585	iii	siconc	Arctic Ocean
5	A	CMCC-ESM2	370, 585	iii	siconc	Arctic Ocean
6	A	CanESM5-1	370, 585	iii	siconc(a)	Arctic Ocean
7	A	CanESM5-CanOE	370, 585	iii	siconc	Arctic Ocean
8	A	CanESM5	370, 585	iii, vi	siconc, sos	Arctic Ocean
9	A	E3SM-1-0	585	iii	siconc	Arctic Ocean
10	A	E3SM-1-1-ECA	585	iii	siconc	Arctic Ocean
11	A	E3SM-1-1	585	iii	siconc	Arctic Ocean
12	A	EC-Earth3-Veg	370, 585	iii	siconc	Arctic Ocean
13	A	FIO-ESM-2-0	585	iii, vi	siconc, tas	Arctic Ocean
14	A	GISS-E2-1-H	585	iii, vi	siconc, sos	Arctic Ocean
15	A	HadGEM3-GC31-LL	585	iii	siconc	Arctic Ocean
16	A	HadGEM3-GC31-MM	585	iii	siconc	Arctic Ocean
17	A	IPSL-CM6A-LR	585	iii	siconc	Arctic Ocean
18	A	MIROC6	585	vi	tas	Arctic Ocean
19	A	MRI-ESM2-0	585	iii, vi	siconc, zos	Arctic Ocean
20	A	NorESM2-MM	585	iii	siconc	Arctic Ocean
21	A	UKESM1-0-LL	370, 585	iii, vi	siconc(a), tas	Arctic Ocean
22	A	UKESM1-1-LL	370	iii, vi	siconc, tas	Arctic Ocean
23	a	CNRM-ESM2-1	245	ii	mlofst_max	Arctic Ocean
24	a	CanESM5-1	119, 245	i	siconc(a), tas	Arctic Ocean
25	a	CanESM5	126, 245	i	siconc	Arctic Ocean
26	a	EC-Earth3-Veg-LR	126	i	siconc	Arctic Ocean
27	a	GISS-E2-1-H	370	i	siconc	Arctic Ocean
28	a	MIROC6	126, 245, 370	i	siconc	Arctic Ocean
29	a	UKESM1-0-LL	126	i	tas	Arctic Ocean
30	B	ACCESS-CM2	585	v, vi	mlofst_max, sos	North Atlantic Ocean
31	B	ACCESS-ESM1-5	585	v	mlofst_max	North Atlantic Ocean
32	B	CESM2-WACCM	126, 245, 585	v	mlofst_max	North Atlantic Ocean
33	B	CESM2	126, 245, 370, 585	v, vi	mlofst_max, sos	North Atlantic Ocean
34	B	CanESM5	585	vi	sos	Baffin Bay
35	B	GISS-E2-1-G	585	v, vi	mlofst_max, sos	Arctic Ocean
36	B	GISS-E2-1-H	585	vi	sos	Arctic Ocean
37	B	GISS-E2-2-G	126, 245	v	mlofst_max	North Atlantic Ocean
38	B	HadGEM3-GC31-MM	585	v	mlofst_max	North Atlantic Ocean
39	B	MRI-ESM2-0	126, 245, 370, 585	v, vi	mlofst_max, sos	Arctic Ocean
40	B	NorESM2-MM	585	v, vi	mlofst_max, sos	North Atlantic Ocean
41	B	UKESM1-0-LL	585	vi	sos	Baffin Bay
42	B	UKESM1-0-LL	585	v	mlofst_max	Norwegian Sea
43	b	CESM2-WACCM	585	ii	sos	North Atlantic Ocean
44	b	GISS-E2-1-G	245, 370	i, ii	sos, tos	North Atlantic Ocean
45	b	GISS-E2-1-H	585	ii	sos	North Atlantic Ocean
46	c	GISS-E2-1-H	119	i	tos	North Atlantic Ocean
47	D	ACCESS-CM2	585	iv	msftmz	North Atlantic Ocean
48	D	ACCESS-ESM1-5	585	iv	msftmz	North Atlantic Ocean
49	D	CESM2-WACCM	126, 585	iv	msftmz	North Atlantic Ocean
50	D	CanESM5	585	iv	msftmz	North Atlantic Ocean
51	D	GISS-E2-1-G	245, 585	iv	msftmz	North Atlantic Ocean
52	D	MIROC-ES2L	585	iv	msftmz	North Atlantic Ocean
53	D	MRI-ESM2-0	126, 245, 585	iv	msftmz	North Atlantic Ocean
54	D	NorESM2-MM	585	iv	msftmz	North Atlantic Ocean
55	D	UKESM1-0-LL	585	iv	msftmz	North Atlantic Ocean
56	E	ACCESS-CM2	585	vi	sos	South Pacific Ocean
57	E	ACCESS-ESM1-5	585	vi	sos	South Pacific Ocean
58	E	CESM2-WACCM	585	vi	sos	South Pacific Ocean
59	E	IPSL-CM6A-LR	585	vi	sos	North Pacific Ocean
60	f	BCC-CSM2-MR	370	ii	mlofst_max	Southern Ocean
61	f	GISS-E2-1-H	119, 126, 245, 370, 585	i, ii	hfds, siconc, tas, tos	Southern Ocean
62	f	GISS-E2-1-H	245, 370	ii	hfds, siconc, tos	Southern Ocean
63	f	HadGEM3-GC31-MM	585	i	siconc	Southern Ocean
64	G	ACCESS-CM2	585	v	mlofst_max	Southern Ocean
65	G	ACCESS-ESM1-5	126, 245, 370, 585	v	mlofst_max	Southern Ocean
66	G	CNRM-CM6-1	245, 370, 585	v	mlofst_max	Indian Ocean
67	G	NorESM2-LM	370, 585	v	mlofst_max	Southern Ocean
68	G	NorESM2-MM	585	v	mlofst_max	Southern Ocean
69	H	CESM2-WACCM	585	vi	msftbarot, zos	Southern Ocean
70	H	IPSL-CM6A-LR	585	vi	zos	Southern Ocean
71	H	MRI-ESM2-0	585	vi	zos	Southern Ocean
72	H	UKESM1-0-LL	585	vi	zos	Southern Ocean
73	I	CanESM5	585	vi	wfo	Southern Ocean

Table A3. List of all 73 SNS and attributes of each SNS. The associated SNS category (cat.) and SSP(s) are listed. The criteria (crit.) and variables (Vars) that are found at least once for each case and associated region are also listed. See text for more information.



#	Passing ensemble members [Variable: SSP119, SSP245, SSP370, SSP585]
1	siconc: -, -, -, 1/10, sos: -, -, -, 1/4
2	siconc: -, -, -, 10/40, tas: -, -, -, 1/40
3	siconc: -, -, -, 1/5, sos: -, -, -, 2/5, zos: -, -, -, 1/5
4	siconc: -, -, 1/1, 1/1, 1/1
5	siconc: -, -, -, 1/1, 1/1
6	siconc: -, -, -, 1/1, 20/20, siconca: -, -, -, 9/20, -
7	siconc: -, -, -, 3/3, 3/3
8	siconc: -, -, -, 50/50, 50/50, sos: -, -, -, 1/50
9	siconc: -, -, -, 4/4
10	siconc: -, -, -, 1/1
11	siconc: -, -, -, 1/1
12	siconc: -, -, -, 1/5, 1/6
13	siconc: -, -, -, 1/1, tas: -, -, -, 3/3
14	siconc: -, -, -, 6/9, sos: -, -, -, 7/8
15	siconc: -, -, -, 4/4
16	siconc: -, -, -, 4/4
17	siconc: -, -, -, 6/6
18	tas: -, -, -, 48/50
19	siconc: -, -, -, 1/5, zos: -, -, -, 1/2
20	siconc: -, -, -, 1/1
21	siconc: -, -, -, 2/10, 5/5, siconca: -, -, -, 1/16, -, tas: -, -, -, 9/14, -
22	siconc: -, -, -, 1/1, -, tas: -, -, -, 1/1, -
23	mlotst_max: -, -, 1/10, -, -
24	siconca: 1/2, -, 1/20, -, -, tas: 1/2, -, -, -
25	siconc: -, 2/50, 1/50, -, -
26	siconc: -, 1/3, -, -
27	siconc: -, -, -, 3/5, -
28	siconc: -, 1/50, 1/50, 1/50, -
29	tas: -, 1/16, -, -, -
30	mlotst_max: -, -, -, 4/10, sos: -, -, -, 1/4
31	mlotst_max: -, -, -, 35/38
32	mlotst_max: -, 1/1, 1/5, -, 3/5
33	mlotst_max: -, 2/3, 1/3, 3/3, 2/3, sos: -, -, -, 1/3
34	sos: -, -, -, 1/50
35	mlotst_max: -, -, -, 4/9, sos: -, -, -, 4/9
36	sos: -, -, -, 7/8
37	mlotst_max: -, 1/5, 2/5, -, -
38	mlotst_max: -, -, -, 4/4
39	mlotst_max: -, 1/1, 1/1, 1/1, 2/2, sos: -, -, -, 2/6
40	mlotst_max: -, -, -, 1/1, sos: -, -, -, 1/1
41	sos: -, -, -, 1/5
42	mlotst_max: -, -, -, 1/5
43	sos: -, -, -, 2/5
44	sos: -, -, 1/20, 2/19, -, tos: -, -, -, 1/19, -
45	sos: -, -, -, 7/8
46	tos: 1/2, -, -, -
47	msftmz: -, -, -, 1/10
48	msftmz: -, -, -, 10/40
49	msftmz: -, 1/1, -, -, 5/5
50	msftmz: -, -, -, 1/49
51	msftmz: -, -, 2/20, -, 5/9
52	msftmz: -, -, -, 1/10
53	msftmz: -, 1/4, 1/4, -, 5/5
54	msftmz: -, -, -, 1/0
55	msfty: -, -, -, 1/5
56	sos: -, -, -, 1/4
57	sos: -, -, -, 9/40
58	sos: -, -, -, 2/5
59	sos: -, -, -, 1/6
60	mlotst_max: -, -, -, 1/1, -
61	hfds: -, 2/9, 4/9, -, 1/9, siconc: -, 4/8, 3/9, 3/5, 6/9, tas: -, 3/8, -, -, -, tos: 1/2, 1/10, 4/10, 1/6, 2/10
62	hfds: -, -, 4/9, 1/5, -, siconc: -, -, 3/9, 3/5, -, tos: -, -, -, 1/6, -
63	siconc: -, -, -, 4/4
64	mlotst_max: -, -, -, 4/10
65	mlotst_max: -, 1/40, 10/40, 34/40, 35/38
66	mlotst_max: -, -, 5/6, 6/6, 6/6
67	mlotst_max: -, -, -, 1/1, 1/1
68	mlotst_max: -, -, -, 1/1
69	msftbarot: -, -, -, 1/5, zos: -, -, -, 1/5
70	zos: -, -, -, 1/6
71	zos: -, -, -, 1/2
72	zos: -, -, -, 1/5
73	wfo: -, -, -, 1/50

Table A4. The same 73 SNS as in Table A3 together with the number of passing ensemble-members per variable, per SSP. See text for further details. When no member passes for an SSP it is denoted as “-”, otherwise it is the number of ensemble-members that fulfil the criteria / the number of available ensemble-members for the model.



Code availability. The framework (Angevaere, 2025) for this work is available at https://github.com/JoranAngevaere/optim_esm_tools. The
645 methods for identifying the criterion iv (subsubsection A1.4, subsection 3.7) are available at <https://github.com/jmecki/AMOCcollapse>

Data availability. The CMIP6 data used in this work is freely available online at <https://esgf-node.llnl.gov/search/cmip6/>

Author contributions. JRA and SSD designed the study, JRA implemented the study, JRA produced the figures, JRA and SSD wrote and edited the paper.

Competing interests. The authors declare no competing interests.

650 *Acknowledgements.* We acknowledge the World Climate Research Programs Working Group on Coupled Modeling, which is responsible for CMIP, and we thank the climate modelling groups (listed in Table A2 of this paper) for producing and making available their model output. For CMIP the U.S. Department of Energy's Program for Climate Model Diagnosis and Intercomparison provides coordinating support and led development of software infrastructure in partnership with the Global Organization for Earth System Science Portals. We thank the climate modelling groups for producing and making available their model output, the Earth System Grid Federation (ESGF) for archiving
655 the data and providing access, and the multiple funding agencies who support CMIP6 and ESGF. The CMIP6 data was accessed and analysed using the Netherlands super-computer-cluster SURFsara.

SSD and JRA received funding from OptimESM and SSD from TipESM. "TipESM "Exploring Tipping Pints and Their Impacts Using Earth System Models" is funded by the European Union. Grant Agreement number: 101137673." OptimESM "Optimal High Resolution Earth System Models for Exploring Future Climate Change" is funded by the European Union. Grant Agreement number:101081193. SSD
660 received funding from ISOTIPIC. "ISOTIPIC" Interacting ice Sheet and Ocean Tipping - Indicators, Processes, Impacts and Challenges" is funded by the National Environmental Research Council, UK, under Grant Number: NE/Y503320/1.



References

- Abbot, D. S., Huber, M., Bousquet, G., and Walker, C. C.: High-CO₂ cloud radiative forcing feedback over both land and ocean in a global climate model, *Geophysical Research Letters*, 36, 2009.
- 665 Angevaare, J. R.: JoranAngevaare/optim_esm_tools: v4.0.0, <https://doi.org/10.5281/zenodo.15275185>, 2025.
- Angevaare, J. R., Drijfhout, S., , and Notz, D.: Newest climate models project much faster disappearance of year-round sea ice in the Arctic, manuscript in preperation, 2025.
- Armstrong McKay, D. I., Staal, A., Abrams, J. F., Winkelmann, R., Sakschewski, B., Loriani, S., Fetzer, I., Cornell, S. E., Rockström, J., and Lenton, T. M.: Exceeding 1.5 C global warming could trigger multiple climate tipping points, *Science*, 377, eabn7950, 2022.
- 670 Bathiany, S., Hidding, J., and Scheffer, M.: Edge detection reveals abrupt and extreme climate events, *Journal of Climate*, 33, 6399–6421, 2020.
- Boers, N.: Observation-based early-warning signals for a collapse of the Atlantic Meridional Overturning Circulation, *Nature Climate Change*, 11, 680–688, 2021.
- Bracegirdle, T. J., Shuckburgh, E., Sallee, J.-B., Wang, Z., Meijers, A. J., Bruneau, N., Phillips, T., and Wilcox, L. J.: Assessment of surface
- 675 winds over the Atlantic, Indian, and Pacific Ocean sectors of the Southern Ocean in CMIP5 models: Historical bias, forcing response, and state dependence, *Journal of Geophysical Research: Atmospheres*, 118, 547–562, 2013.
- Canny, J.: A computational approach to edge detection, *IEEE Transactions on pattern analysis and machine intelligence*, pp. 679–698, 1986.
- De Lavergne, C., Palter, J. B., Galbraith, E. D., Bernardello, R., and Marinov, I.: Cessation of deep convection in the open Southern Ocean under anthropogenic climate change, *Nature Climate Change*, 4, 278–282, 2014.
- 680 Ditlevsen, P. and Ditlevsen, S.: Warning of a forthcoming collapse of the Atlantic meridional overturning circulation, *Nature Communications*, 14, 1–12, 2023.
- Drews, A., Greatbatch, R. J., Ding, H., Latif, M., and Park, W.: The use of a flow field correction technique for alleviating the North Atlantic cold bias with application to the Kiel Climate Model, *Ocean Dynamics*, 65, 1079–1093, 2015.
- Drijfhout, S., Bathiany, S., Beaulieu, C., Brovkin, V., Claussen, M., Huntingford, C., Scheffer, M., Sgubin, G., and Swingedouw, D.: Cata-
- 685 logue of abrupt shifts in Intergovernmental Panel on Climate Change climate models, *Proceedings of the National Academy of Sciences*, 112, E5777–E5786, 2015.
- Drijfhout, S., Angevaare, J. R., Mecking, J., and Rahmstorf, S.: Atlantic overturning collapses in global warming projections after 2100, *researchsquare* (Preprint), <https://doi.org/https://doi.org/10.21203/rs.3.rs-5077014/v1>, 2024a.
- Drijfhout, S. S., Bull, C. Y., Hewitt, H., Holland, P. R., Jenkins, A., Mathiot, P., and Garabato, A. N.: An Amundsen Sea source of decadal
- 690 temperature changes on the Antarctic continental shelf, *Ocean Dynamics*, 74, 37–52, 2024b.
- Feldl, N., Po-Chedley, S., Singh, H. K., Hay, S., and Kushner, P. J.: Sea ice and atmospheric circulation shape the high-latitude lapse rate feedback, *NPJ climate and atmospheric science*, 3, 41, 2020.
- Fox-Kemper, B., Hewitt, H. T., Xiao, C., Adalgeirsdóttir, G., Drijfhout, S. S., Edwards, T. L., Golledge, N. R., Hemer, M., Kopp, R. E., Krinner, G., et al.: Ocean, cryosphere, and sea level change, in: *Climate Change 2021: The Physical Science Basis. Contribution of Working Group I to the Sixth Assessment Report of the Intergovernmental Panel on Climate Change*, pp. 1211–1361, Cambridge University Press, 2021.
- 695 Gómez-Valdivia, F., Holland, P. R., Siahaan, A., Dutrieux, P., and Young, E.: Projected West Antarctic ocean warming caused by an expansion of the Ross Gyre, *Geophysical Research Letters*, 50, e2023GL102978, 2023.



- Hankel, C. and Tziperman, E.: The role of atmospheric feedbacks in abrupt winter Arctic sea ice loss in future warming scenarios, *Journal of Climate*, 34, 4435–4447, 2021.
- Hankel, C. and Tziperman, E.: Assessing the Robustness of Arctic Sea Ice Bi-Stability in the Presence of Atmospheric Feedbacks, *Journal of Geophysical Research: Atmospheres*, 128, e2023JD039337, 2023.
- Hartigan, J. A. and Hartigan, P. M.: The dip test of unimodality, *The annals of Statistics*, pp. 70–84, 1985.
- Heuzé, C.: Antarctic bottom water and North Atlantic deep water in CMIP6 models, *Ocean Science Discussions*, 2020, 1–38, 2020.
- Holland, P. R., Bracegirdle, T. J., Dutrieux, P., Jenkins, A., and Steig, E. J.: West Antarctic ice loss influenced by internal climate variability and anthropogenic forcing, *Nature Geoscience*, 12, 718–724, 2019.
- Hwang, Y.-T. and Frierson, D. M.: Link between the double-Intertropical Convergence Zone problem and cloud biases over the Southern Ocean, *Proceedings of the National Academy of Sciences*, 110, 4935–4940, 2013.
- Jesse, F., Le Bars, D., and Drijfhout, S.: Processes explaining increased ocean dynamic sea level in the North Sea in CMIP6, *Environmental Research Letters*, 19, 044060, 2024.
- Kay, J. E., Holland, M. M., Bitz, C. M., Blanchard-Wrigglesworth, E., Gettelman, A., Conley, A., and Bailey, D.: The influence of local feedbacks and northward heat transport on the equilibrium Arctic climate response to increased greenhouse gas forcing, *Journal of Climate*, 25, 5433–5450, 2012.
- Kopp, R. E., Gilmore, E. A., Shwom, R. L., Adams, H., Adler, C., Oppenheimer, M., Patwardhan, A., Russill, C., Schmidt, D. N., and York, R.: ‘Tipping points’ confuse and can distract from urgent climate action, *Nature Climate Change*, 15, 29–36, 2025.
- Lee, J.-Y., Marotzke, J., Bala, G., Cao, L., Corti, S., Dunne, J., Engelbrecht, F., Fischer, E., Fyfe, J., Jones, C., Maycock, A., Mutemi, J., Niaye, O., Panickal, S., Zhou, T., and Christensen, H.: Future global climate: scenario-based projections and near-term information, pp. 553–672, *IPCC Assessment Reports*, Cambridge University Press, 2021.
- Lenton, T. M., Held, H., Kriegler, E., Hall, J. W., Lucht, W., Rahmstorf, S., and Schellnhuber, H. J.: Tipping elements in the Earth’s climate system, *Proceedings of the national Academy of Sciences*, 105, 1786–1793, 2008.
- Loriani, S., Aksenov, Y., Armstrong McKay, D., Bala, G., Born, A., Chiessi, C. M., Dijkstra, H., Donges, J. F., Drijfhout, S., England, M. H., et al.: Tipping points in ocean and atmosphere circulations, *EGUsphere*, 2023, 1–62, 2023.
- Mchedlishvili, A., Spreen, G., Melsheimer, C., and Huntemann, M.: Weddell Sea polynya analysis using SMOS–SMAP apparent sea ice thickness retrieval, *The Cryosphere*, 16, 471–487, 2022.
- Mecking, J. V. and Drijfhout, S. S.: The decrease in ocean heat transport in response to global warming, *Nature Climate Change*, 13, 1229–1236, 2023.
- Meredith, M. P., Sommerkorn, M., Cassotta, S., Derksen, C., Ekaykin, A. A., Hollowed, A. B., Kofinas, G., Mackintosh, A. N., Muelbert, M. M. C., Melbourne-Thomas, J., et al.: Polar regions, in: *The ocean and cryosphere in a changing climate: Summary for policymakers*, pp. 3–1, *Intergovernmental Panel on Climate Change*, 2019.
- Moreno-Chamarro, E., Caron, L.-P., Loosveldt Tomas, S., Gutjahr, O., Moine, M.-P., Putrasahan, D., Roberts, C. D., Roberts, M. J., Senan, R., Terray, L., et al.: Impact of increased resolution on long-standing biases in HighResMIP-PRIMAVERA climate models, *Geoscientific Model Development Discussions*, 2021, 1–33, 2021.
- Morioka, Y., Manabe, S., Zhang, L., Delworth, T. L., Cooke, W., Nonaka, M., and Behera, S. K.: Antarctic sea ice multidecadal variability triggered by Southern Annular Mode and deep convection, *Communications Earth & Environment*, 5, 633, 2024.
- Munday, D. R., Johnson, H. L., and Marshall, D. P.: Eddy saturation of equilibrated circumpolar currents, *Journal of Physical Oceanography*, 43, 507–532, 2013.



- Naughten, K. A., Holland, P. R., Dutrieux, P., Kimura, S., Bett, D. T., and Jenkins, A.: Simulated twentieth-century ocean warming in the Amundsen Sea, West Antarctica, *Geophysical Research Letters*, 49, e2021GL094566, 2022.
- O'Neill, B. C., Tebaldi, C., Van Vuuren, D. P., Eyring, V., Friedlingstein, P., Hurtt, G., Knutti, R., Kriegler, E., Lamarque, J.-F., Lowe, J.,
740 et al.: The scenario model intercomparison project (ScenarioMIP) for CMIP6, *Geoscientific Model Development*, 9, 3461–3482, 2016.
- Rheinländer, J. W., Smedsrud, L. H., and Nisancioglu, K. H.: Internal ocean dynamics control the long-term evolution of Weddell Sea Polynya activity, *Frontiers in Climate*, 3, 718016, 2021.
- Rose, B. E. and Marshall, J.: Ocean heat transport, sea ice, and multiple climate states: Insights from energy balance models, *Journal of the atmospheric sciences*, 66, 2828–2843, 2009.
- 745 Schulzweida, U.: CDO User Guide, <https://doi.org/10.5281/zenodo.10020800>, 2023.
- Sgubin, G., Swingedouw, D., Drijfhout, S., Mary, Y., and Bennabi, A.: Abrupt cooling over the North Atlantic in modern climate models, *Nature Communications*, 8, 14375, 2017.
- Swingedouw, D., Bily, A., Esquerdo, C., Borchert, L. F., Sgubin, G., Mignot, J., and Menary, M.: On the risk of abrupt changes in the North Atlantic subpolar gyre in CMIP6 models, *Annals of the New York Academy of Sciences*, 1504, 187–201, 2021.
- 750 Taylor, K. E., Stouffer, R. J., and Meehl, G. A.: An overview of CMIP5 and the experiment design, *Bulletin of the American meteorological Society*, 93, 485–498, 2012.
- Terpstra, S., Falkena, S. K., Bastiaansen, R., Bathiany, S., Dijkstra, H. A., and von der Heydt, A. S.: Assessment of Abrupt Shifts in CMIP6 Models using Edge Detection, *arXiv preprint arXiv:2410.19498*, 2024.
- Thompson, A. F., Stewart, A. L., Spence, P., and Heywood, K. J.: The Antarctic Slope Current in a changing climate, *Reviews of Geophysics*,
755 56, 741–770, 2018.
- Våge, K., Papritz, L., Håvik, L., Spall, M., and Moore, G.: Ocean convection linked to the recent ice edge retreat along east Greenland. *Nat. Commun.*, 9, 1287, 2018.
- van Westen, R. M., Kliphuis, M., and Dijkstra, H. A.: Physics-based early warning signal shows that AMOC is on tipping course, *Science advances*, 10, eadk1189, 2024a.
- 760 van Westen, R. M., Vanderborght, E. Y., Kliphuis, M., and Dijkstra, H. A.: Substantial Risk of 21st Century AMOC Tipping even under Moderate Climate Change, *arXiv preprint arXiv:2407.19909*, 2024b.
- Zelinka, M. D., Myers, T. A., McCoy, D. T., Po-Chedley, S., Caldwell, P. M., Ceppi, P., Klein, S. A., and Taylor, K. E.: Causes of higher climate sensitivity in CMIP6 models, *Geophysical Research Letters*, 47, e2019GL085782, 2020.
- Zhang, G. J., Song, X., and Wang, Y.: The double ITCZ syndrome in GCMs: A coupled feedback problem among convection, clouds,
765 atmospheric and ocean circulations, *Atmospheric Research*, 229, 255–268, 2019.